Transition metal sulfides/selenides as cathode electrocatalysts for enhanced hydrogen evolution: Nanostructure engineering strategies and recent

International Journal of Hydrogen Energy 229 (2026) 154736

Contents lists available at ScienceDirect

International Journal of Hydrogen Energy

journal homepage: www.elsevier.com/locate/he

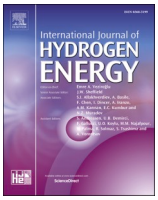

Transition metal sulfides/selenides as cathode electrocatalysts for enhanced hydrogen evolution: Nanostructure engineering strategies and recent progress

Dang Le Tri Nguyen [a,b], Vinh Van Tran [a,b], Chinh Chien Nguyen [c,d], Tung M. Nguyen [e,*]

[a] Laboratory for Advanced Nanomaterials and Sustainable Energy Technologies, Institute for Computational Science and Artificial Intelligence, Van Lang University, Ho Chi Minh City, Viet Nam
[b] Faculty of Applied Technology, Van Lang School of Technology, Van Lang University, Ho Chi Minh City, Viet Nam
[c] Center for Advanced Chemistry, Institute of Research and Development, Duy Tan University, Danang, 550000, Viet Nam
[d] Faculty of Natural Sciences, Duy Tan University, Danang, 550000, Viet Nam
[e] Chemical Engineering, Competence Centre for Catalysis, Chalmers University of Technology, SE-412 96, Gothenburg, Sweden

ARTICLE INFO

Keywords:
Hydrogen evolution reaction
Transition metal sulfides and selenides
Electrocatalysis
Water splitting

ABSTRACT

The depletion of fossil fuels and ecological concerns drive the urgent need for clean energy alternatives. Hydrogen (H_2), with its high energy density and carbon-neutral combustion producing only water, is a promising low-carbon carrier. Traditional methods like methane conversion and coal gasification yield low-purity hydrogen and emit CO_2, pushing for cleaner alternatives such as electrocatalytic water splitting, which relies on efficient electrocatalysts for the hydrogen evolution reaction (HER) to overcome kinetic barriers. Though noble metals like platinum are effective, their cost and scarcity limit use. Transition metal sulfides (TMS) and selenides (TMSe) offer affordable alternatives with unique layered structures, despite challenges like poor conductivity and limited active sites. This review condenses recent nanostructure engineering strategies: morphology and phase engineering, defect engineering and doping, heterostructures, and nanocomposites to boost TMS/TMSe cathode performance for HER, assessing improvements in active site availability, charge transfer, and durability. The recent progress has been examined and explored using contemporary methods, followed by an analysis of the relationship between catalytic performance and the customization of electrocatalysts. The review concludes with insights into recent advancements, identifies and outlines challenges, and prospects for future innovations.

1. Introduction

The severe dependence on fossil fuels - coal, oil, and natural gas - as the primary energy source of the world faces numerous challenges because the combustion of fossil fuels is directly linked to severe environmental degradation and global warming, posing significant challenges to the long-term sustainable development of human civilization [1,2]. Moreover, the rapid depletion of conventional fossil fuels and the mentioned environmental concerns have created an urgent imperative for the development of clean, sustainable, and highly efficient energy sources [3]. Recently, the transition to renewable energy systems has been increasingly recognized as a critical pathway to mitigate climate change and ensure future energy security. Within this evolving energy landscape, hydrogen (H_2) has emerged as an exceptional candidate for a future low-carbon energy system, lauded for its high energy density and carbon-neutral combustion, which produces only water as a byproduct [4–7]. The shift towards hydrogen-based energy is considered vital for addressing contemporary energy and environmental crises. While hydrogen generation is traditionally implemented through methane conversion and coal gasification, these methods yield hydrogen with low purity and emit carbon dioxide [8]. Therefore, a clean, renewable, and efficient technique for H_2 generation without further environmental burden is a key element for the successful realization of a hydrogen economy [9–12].

A promising technology for realizing widespread hydrogen adoption is electrocatalytic water splitting, a process that efficiently produces high-purity hydrogen by applying electrical energy to split water molecules. This process involves two crucial half-reactions: the hydrogen

* Corresponding author at: Chemical Engineering, Competence Centre for Catalysis, Chalmers University of Technology, SE-412 96 Gothenburg, Sweden (Tung M. Nguyen)
E-mail addresses: dang.nlt@vlu.edu.vn (D.L.T. Nguyen), manht@chalmers.se (T.M. Nguyen).

https://doi.org/10.1016/j.ijhydene.2026.154736
Received 24 November 2025; Received in revised form 28 February 2026; Accepted 25 March 2026
Available online 1 April 2026

evolution reaction (HER) at the cathode and the oxygen evolution reaction (OER) at the anode [13]. While the thermodynamic minimum potential required to drive this overall reaction is 1.23 V, practical applications often necessitate higher voltages due to slow reaction kinetics and high overpotentials at the electrode interface. To overcome these kinetic limitations and reduce the energy input, the development of highly efficient and stable electrocatalysts is paramount [14,15]. Currently, noble metal-based catalysts, such as platinum (Pt) and its alloys, represent the state-of-the-art benchmarks for HER due to their superior catalytic activity. However, their high cost, limited natural abundance, and non-renewability severely restrict their large-scale industrial deployment. This economic and scarcity barrier has spurred extensive research into discovering and developing cost-effective, earth-abundant, and robust alternatives to noble metal catalysts [16–18].

In this critical context, various non-precious transition-metal-based catalysts, including chalcogenides, nitrides, phosphides, borides, and carbides, have been extensively explored for HER [5,19–24]. Among these, transition metal sulfides (TMS) and transition metal selenides (TMSe) have emerged as exceptionally promising non-precious metal catalysts for electrocatalytic water splitting [25–28]. These materials are highly valued for their unique layered structures, diverse crystal compositions, and tunable interlayer spacing, features that can be advantageous for facilitating chemical reactions [29–31]. Specifically, their numerous edge sites and potential for sulfur vacancies contribute to their large capacity, while the high polarizability of S^{2-} can facilitate fast ionic transfer. Benefitting from these advantages, TMS and TMSe are increasingly considered promising materials due to their intrinsic properties [32–37]. Their low cost, wide availability, and high HER efficiencies make them significant in the field of 2D electrocatalysts [15,38]. A notable distinction exists between sulfides and selenides, impacting their performance in electrocatalytic applications. Selenides, owing to selenium's lower electronegativity, often exhibit higher electronic conductivity and lower ion migration energy barriers compared to their sulfide counterparts. This intrinsic advantage positions TMSe as particularly attractive for high-performance applications in energy storage and conversion [30,39,40]. However, despite their considerable promise, both TMS and TMSe materials are frequently hampered by inherent limitations that impede their practical applications in electrocatalysis. These drawbacks include inferior electronic conductivity, relatively large ion diffusion energy barriers, poor stability, and insufficient utilization of active sites [41–43]. For instance, early research indicated that bulk molybdenum disulfide (MoS_2) exhibited nearly no activity towards HER, due to its catalytically inert basal plane, with active sites mainly confined to the edge sites [44,45]. This limitation necessitates strategies to maximize the exposure of these active edge sites for their widespread application.

To unlock the full potential of TMS/TMSe materials and address their inherent shortcomings, researchers employ a diverse array of sophisticated nanostructure engineering strategies [46–50], which involve designing and building materials at the nanometer scale to unlock new functions and precisely tailor properties like activity or electronic behavior. This precise control is especially critical in catalysis and electrocatalysis, where engineering the surface area and structure dramatically boosts reaction efficiency and selectivity, driving advancements in sustainable energy like hydrogen production and fuel cells. Unlike bulk TMS/TMSe materials, such as crystalline MoS_2 or WS_2, which exhibit low active site density due to catalysis being confined to edge planes, poor electrical conductivity (particularly in the 2H phase), and sluggish ion/mass transport caused by dense stacking, nanostructured counterparts dramatically overcome these limitations through tailored design. Thus, nanostructure engineering leverages the following key strategies to optimize performance of TMS/TMSe, starting with morphology and phase engineering, which tailors nanoarchitectures like nanowires or nanosheets or three-dimensional structures or core-shell nanoparticles to maximize active edge sites and ensure mechanical integrity, and transforms crystalline phases, such as converting the 2H phase to the metallic 1T phase, to enhance electron transfer and ion intercalation [51–53]. Defect engineering and doping introduce structural imperfections, like sulfur vacancies, and heteroatom doping to create active sites, tune electronic properties, and improve catalytic activity [54,55]. Heterostructure strategies involve crafting interfaces between TMS/TMSe and other materials to promote synergistic charge transfer and structural stability. Nanocomposites, combining TMS/TMSe with conductive carbon-based materials or with complex compositions and structures to enhance electrical conductivity, prevent nanosheet aggregation, and boost HER performance [56–60]. These strategies aim to meticulously tune the nanostructural, electronic, and chemical properties, leading to enhanced catalytic activity, improved ion transport kinetics, and superior long-term stability for energy conversion applications. It has been recognized that these measures are often taken in conjunction with each other to maximize catalytic activity.

Despite significant progress in developing TMS and TMSe as efficient, earth-abundant electrocatalysts for the hydrogen evolution reaction (HER), existing review articles often provide narrow or outdated perspectives. For instance, some focus exclusively on transition metal selenides (TMSe) for HER [61], others limit coverage to sulfides [62], while broader surveys address 2D materials for both photocatalytic and electrocatalytic applications without depth on HER-specific nanostructure engineering [63], and several rely on outdated data [62,64,65]. These limitations leave a gap in a unified, up-to-date overview that specifically emphasizes nanostructure engineering strategies tailored to enhance HER performance in TMS/TMSe cathodes.

This review addresses that need by offering a comprehensive analysis of recent advancements in nanostructure engineering for TMS/TMSe-based cathodes to boost HER electrocatalysis, as illustrated in Fig. 1. Drawing primarily from literature published in the last six years-with particular emphasis on the most cutting-edge studies from the past two years-it synthesizes mechanistic insights into how targeted nanostructural designs (such as defect engineering, heterostructures, and morphology control) directly correlate with improved catalytic activity, kinetics, and stability. By highlighting these correlations and integrating the latest experimental and theoretical findings, the present work complements prior reviews by providing a more focused, timely, and holistic framework that can accelerate research and guide the development of high-performance, non-precious-metal HER catalysts. First, the fundamental mechanisms were examined, emphasizing key factors such as active site density, charge transfer kinetics, and structural stability. The review then systematically evaluates cutting-edge nanostructure engineering approaches: morphology and phase engineering, defect engineering and doping, heterostructures, and nanocomposites, through a curated selection of studies, assessing their impact on catalytic performance and durability. By integrating quantitative comparisons of HER metrics, this work presents a novel framework that bridges the gaps between material design and electrocatalytic functionality. Finally, we address current challenges and propose future research directions, including nanostructure optimization and scalable synthesis methods, to advance TMS/TMSe cathodes for practical energy applications. This review aims to provide a holistic understanding of progress in the field, guide innovative research, and accelerate the adoption of TMS/TMSe-based catalysts in sustainable hydrogen production.

2. Fundamentals and critical aspects for efficient electrocatalysts for HER

2.1. HER mechanisms

The HER is a significant electrochemical process for producing hydrogen gas (H_2) from water, forming the cathodic half-reaction of electrocatalytic water splitting as shown in Fig. 2a. This process is often limited by slow reaction kinetics and high overpotentials, necessitating

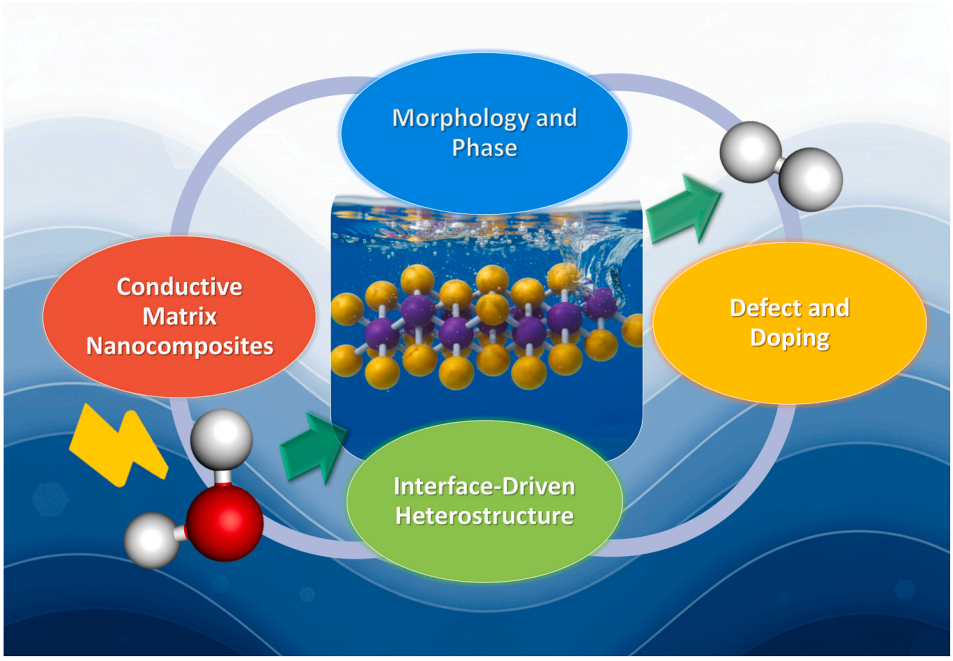

Fig. 1. Illustration of key nanostructure engineering strategies to enhance catalytic electrocatalysts for HER from water splitting.

the development of highly efficient and stable electrocatalysts.

Overall, the HER mechanism typically involves a two-proton-electron pathway, resulting in the reduction of protons (H^+) or water molecules (H_2O) to H_2 gas on an electrode surface under an applied potential (Fig. 2b). The HER proceeds through a series of well-defined steps, beginning with the Volmer step, where a proton (in acidic media) or water molecule (in alkaline/neutral media) combines with an electron at an active site (M) on the catalyst surface to form an adsorbed hydrogen atom (H*) [13,69].

$$\text{In acidic media: } H^+ (aq) + e^- + M \rightarrow M\text{-}H^* \quad (1)$$

$$\text{In alkaline/neutral media: } H_2O + e^- + M \rightarrow M\text{-}H^* + OH^- \quad (2)$$

The subsequent hydrogen desorption can follow either the Heyrovsky or Tafel pathway, depending on the surface coverage of H*. The Heyrovsky step at relatively low H* coverage involves an additional proton (or water molecule) and electron combining with M-H* to release H_2 gas:

$$\text{In acidic media: } M\text{-}H^* + H^+ (aq) + e^- \rightarrow H_2 + M \quad (3)$$

$$\text{In alkaline/neutral media: } M\text{-}H^* + H_2O + e^- \rightarrow H_2 + OH^- + M \quad (4)$$

The Tafel step occurs at high H* coverage; two adjacent M-H* species combine on the electrode surface to desorb H_2 gas. This step occurs in both acidic and alkaline environments.

$$M\text{-}H^* + M\text{-}H^* \rightarrow H_2 + 2M \quad (5)$$

The reaction mechanism and kinetics are heavily influenced by the pH of the electrolyte, the material properties, and the binding energy of adsorbed hydrogen. In alkaline media, the initial water dissociation step can be less efficient compared to acidic conditions, potentially slowing the Volmer step and reducing overall HER performance, which may differ by two to three orders of magnitude due to the slower reduction of H_2O to H_2 alongside OH^- formation. This pH-dependent variation suggests distinct mechanistic pathways, with acidic systems favoring faster rates due to readily available protons, while alkaline systems rely on water reduction. Therefore, optimizing catalysts with various pH conditions is a key area of research.

The rate-determining step (RDS), identified as the slowest among the Volmer, Heyrovsky, or Tafel processes, can be assessed using the Tafel slope, which relates overpotential to current density in a linear fashion within a specific range. Typically, Tafel slopes of 120 mV dec^{-1}, 40 mV dec^{-1}, and 30 mV dec^{-1} correspond to the Volmer, Heyrovsky, and Tafel steps as the RDS, respectively, though real-world complexities often lead to deviations [18,25]. These variations underscore the intricate balance between catalyst structure, electrochemical environment, and reaction kinetics, shaping the efficiency of HER.

Material stability serves as the primary criterion for selecting the electrolyte in TMS/TMSe electrocatalysts for HER. Materials with strong metal-chalcogen bonds and high oxidation resistance, such as MoS_2, WS_2, and their 1T-phase derivatives, are best suited for acidic media, where abundant protons facilitate low overpotentials and rapid kinetics, provided the catalyst withstands dissolution or sulfidation. In contrast, transition metal selenides and bimetallic sulfides, such as $NiSe_2$, NiFe–S, demonstrate superior stability and activity in alkaline media, where hydroxide ions promote efficient water dissociation and reduce corrosion risks compared to acidic environments. Hybrid or doped systems and composites can be engineered for pH-universal performance. This pH-dependent selection ensures optimal catalytic efficiency and operational longevity across diverse electrolytic conditions.

2.2. Theoretical calculations

2.2.1. Key parameters in modeling and calculations

From a fundamental and thermodynamic perspective, driving HER requires overcoming an inherent energy barrier. The thermodynamic minimum potential for overall water splitting is 1.23 V. However, in practice, a higher potential is needed due to overpotential (η), which is the extra energy required to surmount kinetic barriers and achieve a desired reaction rate. Electrocatalysts play a vital role in reducing this overpotential by increasing reaction rates and lowering the energy barriers at each step. A key theoretical descriptor for understanding and designing HER catalysts is the hydrogen binding energy. According to the Sabatier principle, an ideal HER catalyst should have a moderate binding energy with the intermediate H*-neither too strong nor too weak [70]. If the binding is too weak (large positive Gibbs free energy of hydrogen adsorption ΔG_{H^*}), H* has difficulty attaching to the cathode surface, slowing the Volmer step. Conversely, if the binding is too strong

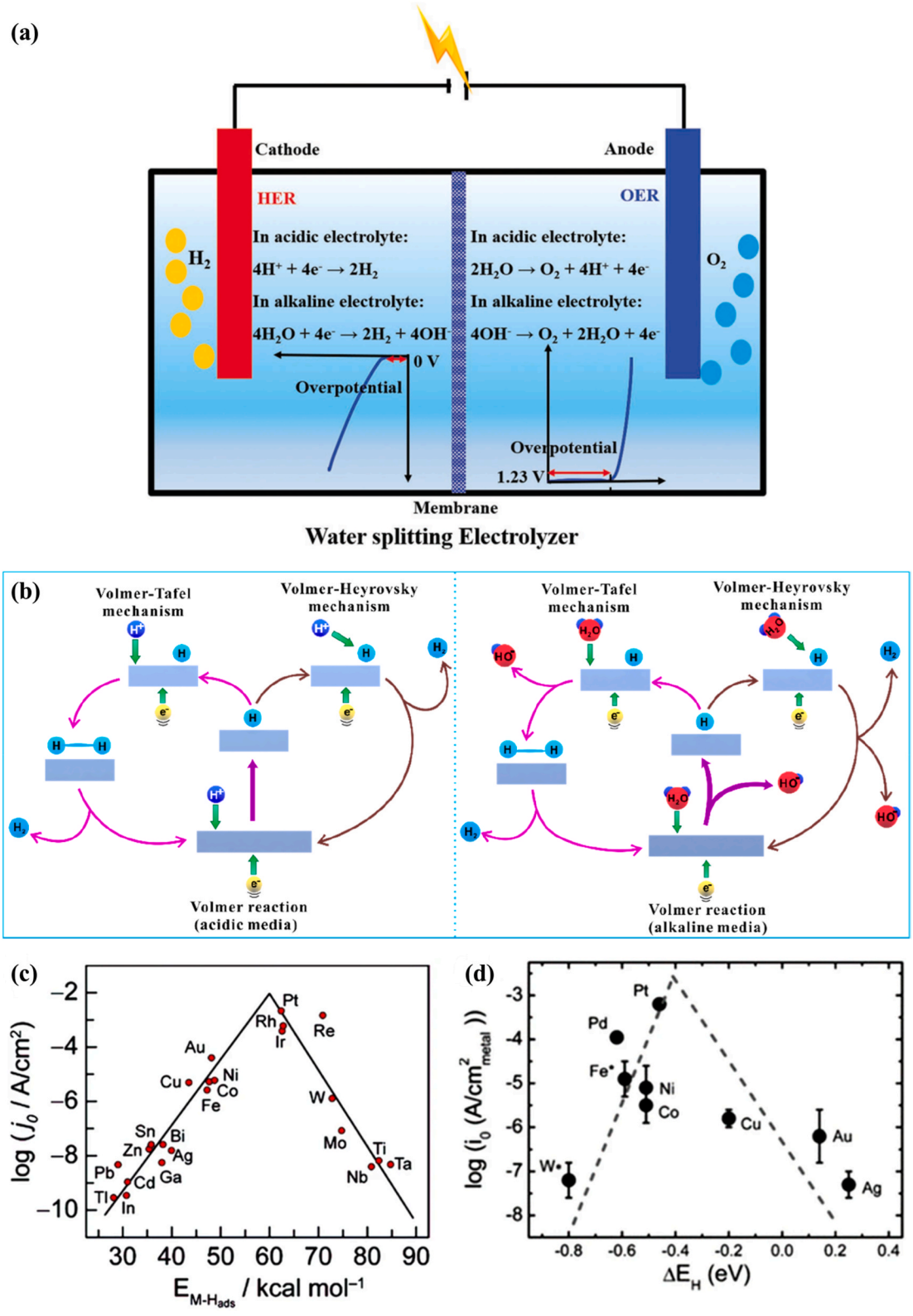

Fig. 2. (a) Schematic illustration of water-splitting electrolyzer and related reaction kinetics. Reused with permission from ref. [13] Wiley-VCH, Copyright© 2019; (b) Mechanism of HER in acidic (left) and alkaline (right) electrolytes. Reused with permission from ref. [14] American Chemical Society, Copyright© 2019; (c and d) Volcano plots: (c) an exchange current density vs. the M−H bond energy (for acidic media). Reused with permission from refs. [66,67], (d) exchange current density on monometallic surfaces vs. the calculated HBE (for alkaline media). Reused with permission from ref. [68] Royal Society of Chemistry, Copyright© 2013.

(large negative ΔG_{H^*}), the formed H_2 product struggles to desorb, potentially blocking active sites and halting the reaction [71]. Therefore, the optimum value is close to zero* [72]. This relationship is famously visualized in "volcano plots", shown in Fig. 2c and d, where catalysts with ΔG_{H^*} values closest to the peak (near zero) demonstrate the highest catalytic activity (e.g., platinum, Pt).

Density functional theory (DFT) calculations are crucial for revealing the interaction between different components and optimizing the intrinsic activity of electrocatalysts by manipulating the morphology and construction. Typically, DFT calculations are extensively used to estimate ΔG_{H^*} values, providing a theoretical basis for screening potential HER electrocatalysts. For example, by simulating interfaces between different material components, DFT reveals how defects, such as vacancies, enhance hydrogen adsorption by straining active sites, achieving an optimal $\Delta G_{H^*} \approx 0$ eV [73,74]. For nanostructured TMS/TMSe, DFT studies the effects of particle size, layer thickness, edge sites, doping, and single-atom catalysts on the electronic structure, tuning ΔG_{H^*} to enhance catalytic efficiency [3,45,75–77]. It also compares catalytic activity across crystalline phases, such as the semiconducting 2H versus the metallic 1T phase of MoS_2 or $MoSe_2$, with the 1T phase often showing superior conductivity and more favorable ΔG_{H^*} values, making it more catalytically active than the 2H phase [26,78,79].

For transition metal-based catalysts, the d-band center theory (εd), developed by Nørskov and co-workers, further links the H* adsorption strength and ΔG_{H^*} to the surface electronic structures, particularly the d-orbital levels of the metal atoms [80,81]. A d-band center closer to the Fermi level generally indicates stronger adsorption, while one further away suggests weaker adsorption [82]. Modulating these electronic structures, often by inserting non-metal atoms (like S, P, N) or through doping and heterostructure formation, can weaken strong metal-hydrogen bonds (e.g., Mo–H) and optimize HER performance [83,84]. Furthermore, density of states (DOS) plots are used to confirm charge transfer, electron filling in bonding/antibonding states, and the enhancement of hydrogen intermediate desorption [85,86]. These simulations guide the rational design of catalysts by predicting how structural modifications minimize overpotential and maximize HER activity. Ultimately, DFT-driven insights into ΔG_{H^*} enable the development of efficient, sustainable TMS/TMSe electrocatalysts for industrial hydrogen production.

2.2.2. Conditions for simulation

To enhance the HER performance of transition metal sulfide and selenide (TMS/TMSe) electrocatalysts, DFT calculations provide a theoretical framework for understanding catalytic processes, and the resulting values, such as ΔG_{H^*}, are derived from specific computational conditions. ΔG_{H^*} is determined by modeling the intermediates formed during HER processes, encompassing hydrogen adsorption, reduction, and desorption on the catalyst surface, using the equation:

$$\Delta G_{H^*} = \Delta E_{H^*} + \Delta E_{ZPE} - T\Delta S \quad (6)$$

Where ΔE_{H^*} represents the energy change relative to the reference state of separated H_2 molecules. Meanwhile, ΔE_{ZPE}, the zero-point energy change for adsorbed H* and isolated H_2, is derived from vibrational frequency calculations to account for quantum mechanical effects [14,87].

The electrolyte is a critical factor determining the efficiency of electrochemical water splitting, which depends on the simultaneous performance of both the HER and the OER electrocatalysts in a practical two-sided reaction. A major challenge is that most non-noble-metal catalysts cannot efficiently catalyze both reactions under the same conditions, as HER promoters prefer acidic media while OER catalysts favor alkaline media. This disparity makes developing highly effective and efficient HER catalysts for alkaline media extremely crucial, especially since catalytic materials typically exhibit lower activity in alkaline solutions than in acidic ones, even though catalysts are often less stable in acidic conditions [8,14,88]. Therefore, in acidic media, DFT focuses on proton reduction, employing ΔG_{H^*} and the d-band center as primary descriptors, while in alkaline media, the rate-limiting Volmer step (water dissociation) necessitates modeling the Gibbs free energy of water adsorption (ΔG_{H2O^*}) [89]. For example, DFT studies demonstrate that N-doped $NiSe_2$ achieves lower ΔG_{H^*} and ΔG_{H2O^*} values, significantly enhancing alkaline HER activity compared to pristine materials [90].

2.3. Some critical parameters in HER

To reliably evaluate HER electrocatalysts, several critical parameters are rigorously investigated:

Overpotential (η): This is the primary metric, representing the excess potential beyond the thermodynamic minimum (1.23 V for overall water splitting) required to drive the reaction at a specific current density. Commonly reported values include η_{10} (overpotential at 10 mA cm^{-2}), which is often used for comparison as it correlates to 12.3% solar-to-hydrogen efficiency, and η_{500} or η_{1000} for industrial-scale hydrogen production. A smaller η indicates higher catalytic activity and lower energy consumption. It is popular to perform *iR* compensation to correct for ohmic potential drops from internal resistance, solvent resistance, and contact resistance, especially at high current densities, to accurately assess intrinsic catalytic activity.

Tafel Slope (*b*): This parameter is derived from the linear region of a Tafel plot (overpotential vs. logarithm of current density) and provides insight into the HER reaction mechanism and its rate-determining step (RDS). Different RDSs correspond to distinct Tafel slope values: approximately 120 mV dec^{-1} for the Volmer reaction, ~40 mV dec^{-1} for the Heyrovsky reaction, and ~30 mV dec^{-1} for the Tafel reaction. A smaller Tafel slope indicates faster electron-transfer kinetics and a lower overpotential required for the same current density increment. Platinum (Pt) is the benchmark, exhibiting one of the smallest Tafel slopes, around ~ 33 mV dec^{-1}.

Electrochemical Impedance Spectroscopy (EIS): EIS is used to study the kinetics of adsorption and desorption processes and to evaluate the conductivity of catalysts. It measures changes in capacitance and interfacial electron-transfer resistance (R_{ct}) at the electrode surface. A smaller R_{ct} value suggests a faster reaction rate and lower overpotential. The adsorption resistance (R_{ad}) obtained from Nyquist plots reflects the onset potential of HER, with smaller R_{ad} values indicating a more positive onset potential.

Stability/Durability: For practical applications, catalysts must maintain their performance over extended periods. Stability is typically assessed through chronoamperometry (CA), where current density is held constant (e.g., 10-500 mA cm^{-2}) while monitoring potential variations over extended durations (e.g., >10-100 h, or up to 1000 h for industrial relevance); appropriate analysis includes quantifying voltage drift (ideally <5-10% increase), post-CA characterizations (e.g., XPS, TEM, or EIS) to detect structural/chemical degradation like phase changes or dissolution, and comparison with initial metrics to confirm retained activity. Complementary methods involve chronopotentiometry, which tracks potential at fixed current for similar timeframes, and accelerated stress testing via cyclic voltammetry (CV), comparing polarization curves before and after 1000-5000 cycles, with minimal overpotential shifts or current decay indicating excellent durability against aggregation, corrosion, or mechanical failure.

Faradaic Efficiency (FE): FE is a critical metric for confirming that electrons are selectively used for H_2 production rather than side reactions, typically exceeding 95–99% in well-optimized TMS/TMSe HER catalysts across a wide current range. However, unlike CO_2 reduction, where parasitic processes and various products frequently lower FE and make it a central reporting parameter, FE is less commonly emphasized in HER literature because the reaction is inherently selective in most aqueous electrolytes, with minimal competing pathways under standard

conditions. Nevertheless, reporting FE, validated by gas quantification versus charge passed, remains valuable for HER in challenging media like seawater or neutral pH, where Cl^- oxidation or impurity effects can reduce efficiency and must be explicitly addressed.

Turnover Frequency (TOF): TOF quantifies the intrinsic catalytic activity, defining the number of product molecules (H_2) formed per catalytic site per unit time. While challenging to calculate precisely for complex materials, especially hybrids or heterostructures, TOF remains a valuable metric for comparing catalytic efficiencies, particularly within similar systems. For HER, the number of electrons transferred (n) is 2 for H_2 formation.

Electrochemical Active Surface Area (ECSA) and Double-Layer Capacitance (C_{dl}): ECSA reflects the actual surface area of the catalyst exposed to the electrolyte, often determined from C_{dl} measurements. Normalizing current density by ECSA before determining overpotential values is crucial for evaluating intrinsic catalytic activity and avoiding errors caused by variations in catalyst loading.

These parameters, alongside advanced characterization techniques and theoretical calculations like DFT, are indispensable for deeply understanding reaction mechanisms, optimizing catalyst design, and bridging the gap between theoretical insights and practical applications in sustainable hydrogen production.

3. Recent advances in TMS and TMSe electrocatalysts for HER

3.1. Morphology and phase engineering

Morphology engineering is considered a commonly used strategy aimed at finely tuning the shape, size, and structural architecture of transition metal sulfides and selenides to enhance active site availability, boost charge transport efficiency, and improve overall stability. This technique involves a variety of nanostructures, such as two-dimensional (2D) nanosheets, one-dimensional (1D) nanorods, and intricate designs like porous or hollow frameworks (3D), each tailored to maximize catalytic performance [63,91–96]. Beyond morphology, phase engineering plays a critical role by manipulating the crystal phases, for instance, transitioning from the semiconducting 2H phase to the metallic 1T or 1T' phases, which can significantly alter their electronic properties, catalytic activity, and stability for the HER [97,98]. Recent advancements have been chosen and discussed on innovative and unique nanostructures, integrating phase engineering to optimize HER efficiency by leveraging the synergistic effects of phase transitions and morphological diversity.

2D transition metal dichalcogenides (TMDs), including nanosheets, provide a notable advantage due to their extensive surface area and layered configuration, leading to reduced overpotentials and lower Tafel slopes for the HER. This inherent structural benefit continues to fuel significant research into 2D structures. Beyond merely increasing surface area, recent developments emphasize creating tailored architectures that improve electron and mass transport pathways while boosting structural durability under challenging reaction environments [94,99]. For example, Wang's group initially prepared vertically oriented MoS_2 and WS_2 nanosheets that boast high activity in the HER. This distinctive layer arrangement not only provides maximum exposure of active edge sites but also ensures rapid removal of small gas bubbles, thus maintaining an expansive and effective working surface [100]. Besides, the edge-site approach holds significant potential for designing efficient catalysts. Singh's group used DFT to emphasize the critical role of edge sites in the adsorption and dissociation of water on 2D monolayer MoS_2, with the Mo-edge (0% sulfur coverage) identified as the most catalytically active due to its undercoordinated Mo atoms, which facilitate strong interactions with H_2O, OH, and H species [101]. These edge sites lower the activation energy barrier for water dissociation to 0.54 eV, significantly less than the 2.31 eV on the S100-edge (100% sulfur coverage) and 0.82 eV on the S50-edge (50% sulfur coverage), enabling spontaneous dissociation at room temperature with a free energy barrier as low as 0.06 eV under certain conditions. The enhanced reactivity at the Mo-edge, compared to the inert basal plane, arises from its ability to form stable bonds with dissociated species and its favorable thermodynamic and kinetic profile, underscoring the importance of edge engineering for optimizing MoS_2. Later, Li et al. employed CVD to create nanostructured 2D MoS_2 thin films. By tuning CVD parameters, an optimized MoS_2 structure can be achieved. This structure is characterized by large MoS_2 platelets that serve as a base, with smaller, layered MoS_2 sheets growing perpendicularly from them. This unique arrangement effectively increases the total number of active edge sites within a given geometric area, which is crucial for enhancing catalytic performance [102].

Using surfactants to control and optimize the morphology and phase of electrocatalysts also demonstrated an excellent improvement in the catalyst's performance. Li et al. utilized hexadecyl trimethyl ammonium bromide (CTAB) and polyethylene-polypropylene glycol (F68) to synthesize $MoSe_2$-CTAB@F68 electrocatalyst (Fig. 3) with uniform, ultrasmall, few-layered nanosheets evenly distributed, and the smallest nanoscale sizes compared to samples without surfactants or with single surfactants [103]. The electrocatalyst $MoSe_2$-CTAB@F68 exhibited an enhanced HER performance with an overpotential of 189 mV at 10 mA cm^{-2} and a Tafel slope of 62 mV dec^{-1} in 0.5 M H_2SO_4 electrolyte. This superior performance is attributed to the synergistic effect of dual surfactants, which expanded the interlayer spacing to 0.69 nm, increased the active surface area, and improved hydrophilicity. Compared to 2H–$MoSe_2$ (no surfactant), $MoSe_2$-CTAB@F68 showed a lower overpotential (189 mV vs. 240 mV) and reduced Tafel slope (62 vs. 82 mV dec^{-1}), highlighting the benefits of morphology engineering. Moreover, the dual-surfactant approach (5:5 M ratio) outperformed single-surfactant variants like $MoSe_2$-CTAB and $MoSe_2$–F68 by providing more active sites and faster kinetics. XPS analysis indicated a 0.6 eV shift to lower binding energies for Mo 3d and Se 3d peaks in $MoSe_2$-CTAB@F68, suggesting higher electron density around active sites that facilitates hydrogen adsorption and desorption. Overall, the study demonstrates that dual surfactants enable precise control over $MoSe_2$ morphology, leading to excellent stability over 2000 cycles and highlighting the synergy in tuning hydrophilicity, spacing, and sites.

Besides, various cutting-edge nanostructures, including 1D nanorods and 3D nanoflowers, have been shown to significantly boost the efficiency of the HER, opening new avenues for advanced electrocatalytic applications [58,105–109]. For instance, Nguyen et al. developed various morphologies for WS_2- and WO_3-based composite catalysts using a straightforward batch reactor method, successfully creating WO_3 nanorods (WO_3 NR), WS_2/WO_3 nanobricks (WS_2/WO_3 NB), and WS_2/WO_3 nanorods (WS_2/WO_3 NR) [106]. The structures, compositions, and properties of these materials were thoroughly analyzed and verified, demonstrating their potential for HER. The 1D WS_2/WO_3 NR exhibited significantly enhanced electrocatalytic performance, evidenced by a lower Tafel slope of 82.7 mV dec^{-1} for WS_2/WO_3 NR compared to 112.5 mV dec^{-1} for WO_3 NR and 195.5 mV dec^{-1} for WS_2/WO_3 NB, alongside a reduced resistance of 397.7 Ω versus 1816 Ω and 3597 Ω for the other two, respectively. In another study, this group continued developing innovative catalysts by introducing a simple, scalable process to synthesize a nanoflower (NF) of MoS_2 and WS_2 (MoS_2/WS_2 NF), leveraging the high catalytic potential of transition metal dichalcogenides (TMDs) like MoS_2 and WS_2 [107]. The 3D MoS_2/WS_2 NF showed superior HER activity with a low overpotential of 251 mV at 10 mA cm^{-2}, a small Tafel slope of 61 mV dec^{-1}, excellent conductivity, and remarkable stability, highlighting the benefits of the WS_2–MoS_2 NF morphology. Very recently, Zhao et al. synthesized $NiSe_2$/CoSe/nickel foam (NF) electrocatalysts featuring a 3D microflower structure, facilitated by varying NH_4F molar ratios, with the $NiSe_2$/CoSe/NF-3.0 electrode demonstrating the highest HER efficiency [110]. This catalyst delivered an overpotential of 148 mV at 10 mA cm^{-2} and a Tafel slope of 88.6 mV dec^{-1} in 1 M KOH, attributed to the greater exposure of active sites, improved electron movement, and interactions

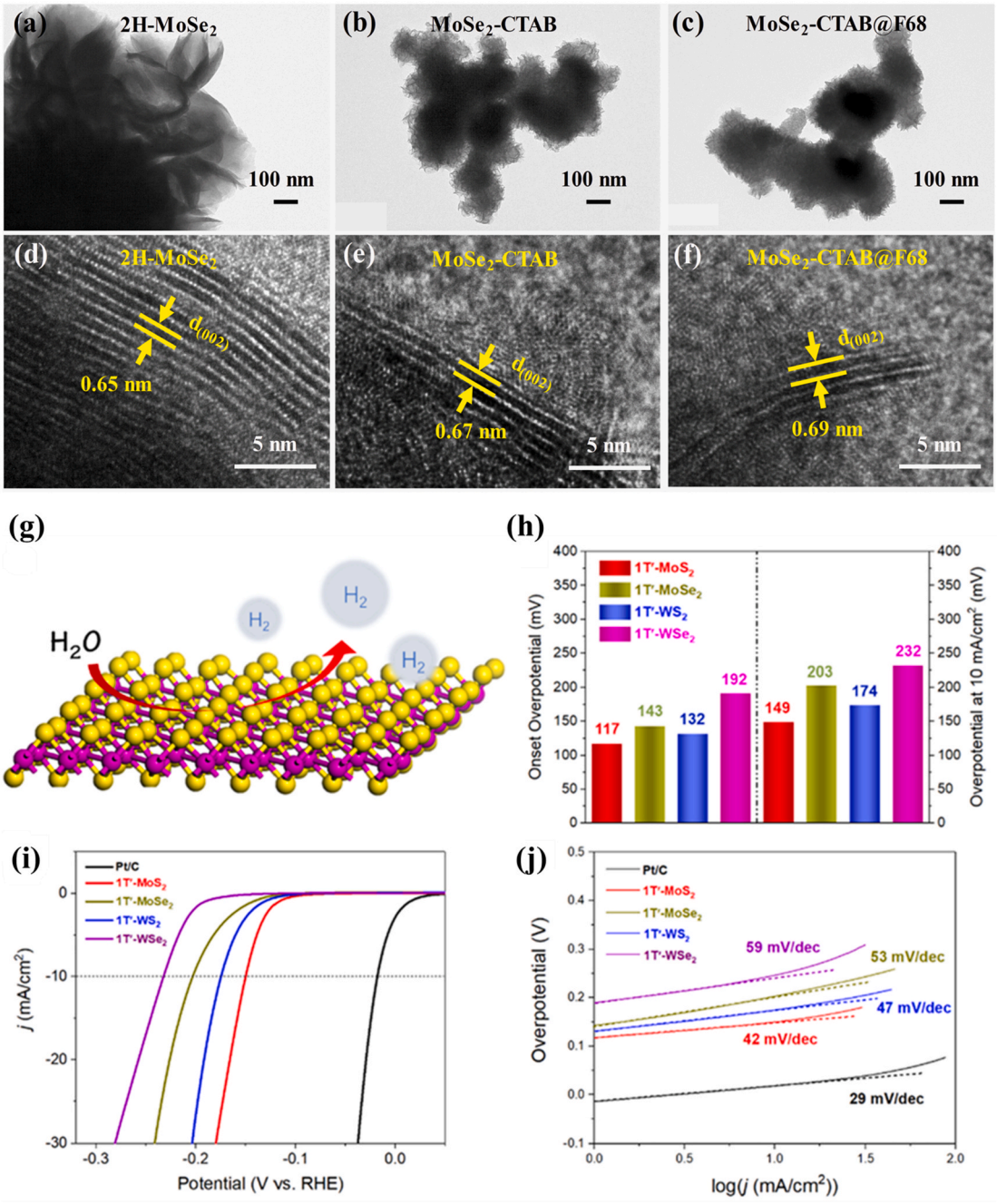

Fig. 3. (a-c) TEM images, (d–f) HRTEM images, and HER performance of 2H–$MoSe_2$, $MoSe_2$-CTAB, and $MoSe_2$-CTAB@F68. Reused with permission from ref. [103] Elsevier, Copyright© 2021. (g) Schematic diagram of the 1T′-TMD nano-monolayers for HER, (h) Polarization curves. (i) Onset overpotential (left axis) and overpotential at 10 mV cm^{-2} (right axis), (j) Tafel plots of 1T′-MoS_2, 1T′-$MoSe_2$, 1T′-WS_2, 1T′-WSe_2, and Pt/C. Reused with permission from ref. [104] American Chemical Society, Copyright© 2022.

between $NiSe_2$ and CoSe. DFT analyses indicated that the $NiSe_2$/CoSe interface enhances electron density near the Fermi level and reduces the d-band center, boosting H* desorption and HER reaction rates. The superior HER performance is reinforced by a large electrochemically active surface area and a minimal charge transfer resistance, underscoring the value of morphological adjustments in enhancing catalytic effectiveness.

Polymorphic and phase engineering is considered an effective strategy to enhance the catalytic performance of TMDs by optimizing their electronic and structural properties [104,111–113]. Particularly, for the 1T′ phase, which is known for its metallic character and superior HER activity compared to the semiconducting 2H phase. However, synthesizing pure bulk 1T′-phase TMDs poses significant challenges due to their high formation energy, requiring complex and high-temperature processes, which can complicate scalability and control. Additionally, the development of high-phase-purity 1T′-TMD monolayers under mild conditions remains rare, as it involves overcoming the van der Waals forces between layers and maintaining phase stability, making it a less explored area of research. To address this, a novel colloidal synthesis strategy has been developed, enabling the high-yield production of well-defined, nano-monolayer, high-phase-purity 1T′-TMD nanosheets, including 1T′-MoS_2, 1T′-$MoSe_2$, 1T′-WS_2, and 1T′-WSe_2 [104]. The 1T′-phase structure, exemplified by 1T′-MoS_2, was verified and confirmed by advanced characterization techniques, specifically: TEM,

HRTEM, XPS, Raman spectroscopy, and XANES/EXAFS. As a proof-of-concept, these 1T′-TMD nano-monolayers, particularly 1T′-MoS_2, demonstrated exceptional electrocatalytic activity for HER, achieving a low overpotential of 149 mV at 10 mA cm^{-2} and a Tafel slope of 42 mV dec^{-1}, with excellent durability. The superior HER performance is attributed to the exposure of conductive basal planes and increased edge sites in the nanosized monolayers, enhanced by lattice strain.

Otherwise, Kwon et al. synthesized nonstoichiometric $MoSe_x$ (x = 1.8, 2.0, 2.2, 2.3, 2.4) nanosheets via a hydrothermal reaction, controlling the 2H-to-1T′ phase transition by adjusting the Se/Mo ratio, with the 1T′ phase dominating when x exceeded 2, and $MoSe_{2.3}$ showing the best HER performance in 0.5 M H_2SO_4 with a current of 10 mA cm^{-2} at 130 mV vs RHE and a Tafel slope of 46 mV dec^{-1} [112]. Detailed

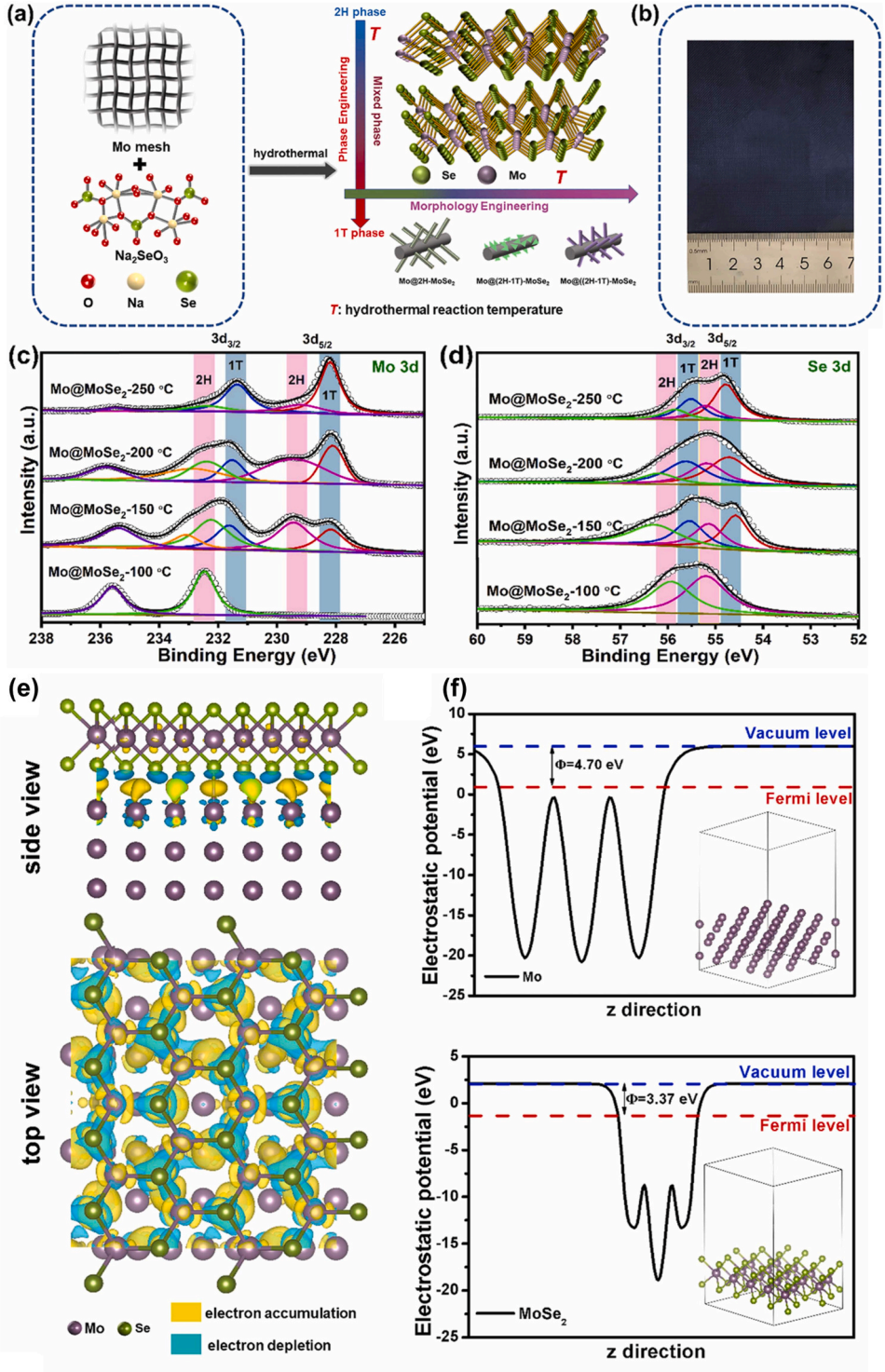

Fig. 4. (a) Schematic diagram of phase and morphology-controlled synthesis of $MoSe_2$ via hydrothermal in-situ etching process, (b) photograph of the as-prepared Mo@(2H-1T)-$MoSe_2$ catalyst with dimensions of 7 × 8 cm^2, (c, d) high-resolution XPS spectra of Mo@$MoSe_2$ prepared at different reaction temperatures (c) Mo 3d and (d) Se 3d, (e) the charge density distribution at the interface of the Mo@(2H-1T)-$MoSe_2$ heterostructure, (f) the electrostatic potential calculations of Mo metal (top) and $MoSe_2$ (bottom). Reused with permission from ref. [115] Elsevier, Copyright© 2022.

imaging and chemical analyses (HAADF-STEM, EXAFS, and XPS) revealed that extra selenium (Se) atoms created bonds with each other and that some molybdenum (Mo) atoms were missing in the structure. Advanced calculations suggested two stable forms of the 1T' phase, one where extra Se atoms connect layers, and another where Se replaces Mo and additional Se atoms fill in gaps, with the latter showing the most effective sites for the HER. These findings unveil how excess Se not only drives the phase conversion but also enhances catalytic activity, offering insights into optimizing Se-rich $MoSe_2$ for improved HER performance. Similarly, Shaikh et al. synthesized highly disordered 2D-MoS_2 nanosheets, where an excess of sulfur in the precursor led to diverse morphologies and enhanced physicochemical properties [114]. The S-rich $MoS_{2+\delta}$ nanosheets, characterized by a high density of ripples and wrinkles, exhibited an optimal HER performance with a low overpotential of 234 mV at 10 mA cm^{-2} and a Tafel slope of 82 mV dec^{-1} in acidic conditions, supported by DFT calculations that explored various sulfur configurations to elucidate their impact on hydrogen absorption and desorption.

In another study, Yang et al. implemented a hydrothermal in-situ etching technique to create the Mo@(2H-1T)-$MoSe_2$ monolithic electrode using a Na_2SeO_3 solution, producing a configuration with nanosheets layered on the Mo mesh and a thickness of approximately 6.4 nm, contrasting with nanorods or nanotubes formed under varying temperatures [115] (Fig. 4). The Mo@(2H-1T)-$MoSe_2$ electrocatalyst demonstrated an overpotential of 183 mV at 20 mA cm^{-2} and a Tafel slope of 72 mV dec^{-1} in an acidic electrolyte, and also showcased excellent activity across all pH levels. This enhanced performance is credited to the combined influence of the mixed 2H-1T phases of $MoSe_2$ nanosheets. Relative to Mo mesh and Mo–$MoSe_2$, the Mo@(2H-1T)-$MoSe_2$ exhibited reduced overpotentials and lower Tafel slopes, underscoring the advantages of phase and structural optimization. The electrode's electrochemical surface area (ECSA) reached 70.2 mF cm^{-2}, markedly surpassing that of Mo mesh and Mo–$MoSe_2$, owing to the increased active sites. Real-time electrochemical impedance spectroscopy (EIS) and DFT analyses verified improved electron mobility and decreased charge transfer resistance (Rct) in Mo@(2H-1T)-$MoSe_2$, boosting HER reaction rates. Interestingly, in seawater, the electrocatalyst recorded an overpotential of 470 mV at 20 mA cm^{-2} with a Tafel slope of 196 mV dec^{-1}, outperforming its counterparts, while maintaining durability over 12 h and 1000 cycles. Remarkably, the piezo-flexoelectric coupling effect, arising from the interfacial strain between the 2H and 1T phases of $MoSe_2$, creates internal electric fields that promote electron transfer and hydrogen intermediate (H*) adsorption, which is crucial for overcoming the corrosive chloride environment of seawater. The nanosheet morphology, with a thickness of 6.4 nm, provides a high electrochemical surface area, ensuring abundant effective active sites mainly induced by the morphology effect, which resist deactivation by Mg/Ca precipitates. This structure minimizes corrosion and poisoning from seawater impurities, maintaining nearly 100% FE and stability over 12 h. Besides, the Mott-Schottky heterojunction further enhances charge redistribution, accelerating H–OH bond breaking and H* formation, making Mo@(2H-1T)-$MoSe_2$ robust for seawater electrolysis. This combination of phase engineering, morphology optimization, and heterojunction effects ensures high activity and durability in harsh seawater conditions.

This section highlights that morphology and phase engineering are synergistic strategies for boosting HER performance in TMS/TMSe catalysts. Morphology optimization - such as vertical 2D nanosheets, edge-rich layered structures, ultra-small few-layered sheets via dual surfactants, 1D nanorods, or 3D nanoflowers/microflowers - primarily increases active site exposure (especially edges), improves mass/charge transport, enhances hydrophilicity, and facilitates bubble detachment. Phase engineering, particularly shifting from semiconducting 2H to metallic 1T/1T′ phases, activates basal planes, dramatically improves conductivity, and optimizes electronic structure (e.g., lower ΔG_{H^*}, downshifted d-band center). The most effective catalysts combine both approaches, as seen in high-purity 1T′-TMD nano-monolayers (149 mV overpotential, 42 mV dec^{-1}), Se-rich $MoSe_{2.3}$ (130 mV, 46 mV dec^{-1}), and mixed 2H-1T $MoSe_2$ with piezo-flexoelectric effects for seawater tolerance. A key design rule is that morphology boosts extrinsic factors (ECSA, kinetics pathways), while phase engineering targets intrinsic activity, and their integration yields the lowest overpotentials and Tafel slopes. However, inherent trade-offs often balance enhanced activity against potential reductions in long-term stability or synthesis simplicity. With this strategy, the phase engineering approach shifts materials to metallic 1T/1T′ phases for superior conductivity and basal-plane activity, yielding low overpotentials and Tafel slopes, but these metastable phases demand high-energy or complex processes that can compromise structural durability, as seen in the challenges of maintaining 1T′ purity without aggregation or phase reversion.

3.2. Defect and doping

The impact of vacancies, such as sulfur and selenium, significantly enhances catalytic performance. These vacancies generate additional active sites for hydrogen adsorption, water dissociation, effectively reducing the energy barrier and accelerating reaction kinetics [116–118]. They also alter the electronic structure by adjusting the Fermi level and d-band center, optimizing the binding energy of hydrogen intermediates to enhance efficiency. Improved charge transfer is another key advantage, as defect-induced electronic states enable smoother electron movement during the reaction. This effect is especially pronounced in materials where modified defect states increase overall conductivity [119]. Structural analyses further indicate that these vacancies cause lattice distortions, boosting the availability of catalytic sites [120]. Various methods, including thermal annealing, argon plasma treatments, and ion beam irradiation, have been employed to introduce surface sulfur vacancies [121–124]. Together, these factors contribute to a more effective and stable hydrogen evolution process. Consequently, ongoing research continues to explore these vacancy effects, fueling innovations in catalyst design for sustainable energy solutions.

Yin et al. explore the HER catalytic activity of porous molybdenum disulfide (MoS_2) nanosheets [125], highlighting the critical role of sulfur vacancies (S-vacancies) alongside phase and edge sites, with the porous 1T-phase MoS_2, featuring a high S-vacancy concentration, achieving an overpotential of 153 mV vs. RHE for a current density of 10 mA cm^{-2}. Using electron spin resonance (ESR) and positron annihilation lifetime spectroscopy (PALS), the research quantifies S-vacancies, revealing their significant contribution to enhanced HER performance, as seen in the reduced Tafel slope of 43 mV per decade when S-vacancies are optimized. Otherwise, Li et al. examine the role of S-vacancies and undercoordinated Mo regions in enhancing HER performance of multilayered MoS_2 nanosheets, identifying two distinct stages: "point defects" at low S-vacancy concentrations (S:Mo $>$ 1.7) and undercoordinated Mo regions at high concentrations (S:Mo $<$ 1.7) due to sulfur stripping. The study employed modern techniques such as TEM, EPR, and XPS to verify that sulfur vacancies and undercoordinated molybdenum atoms enhance catalytic performance by expanding the number of active sites and accelerating reaction kinetics. Amorphous MoS_2 showed the highest HER activity in acidic media with a minimal overpotential of ~100 mV and a Tafel slope of 44 mV dec^{-1}, while defective 2H MoS_2, particularly MoS_2–7H with extensive S-vacancies, performed best in alkaline media with a turnover frequency (TOF) of ~2 s^{-1} at 160 mV overpotential with a Tafel slope reducing to approximately 80 mV dec^{-1}, reflecting enhanced HER kinetics.

Patasinska's group explored the reactivity of sulfur vacancy-rich MoS_2 surfaces toward water dissociation, utilizing an Ar^+ ion beam sputtering technique to create exposed Mo sites that enhance catalytic activity [117]. In situ near-ambient pressure X-ray photoelectron spectroscopy (NAP-XPS) and density functional theory (DFT) analyses revealed that these defective surfaces facilitate dissociative adsorption of water, producing oxides, hydroxides, chemisorbed, and physisorbed

H_2O molecules, highlighting the role of exposed Mo sites in enhancing water-splitting efficiency on MoS_2 surfaces treated with Ar^+ ion sputtering (Fig. 5a and b). The ultraviolet photoelectron spectroscopy (UPS) confirmed the metallic character of the MoS_2 surface post-sputtering, supporting its catalytic potential without transitioning from the 2H to 1T phase. This work provides valuable insights into optimizing MoS_2 for hydrogen production through simple surface engineering, opening avenues for further research into sustainable energy solutions. In another recent study, Fruehwald et al. developed a series of monolayer MoS_2 electrocatalysts using chemical vapor deposition, introducing nanoscale

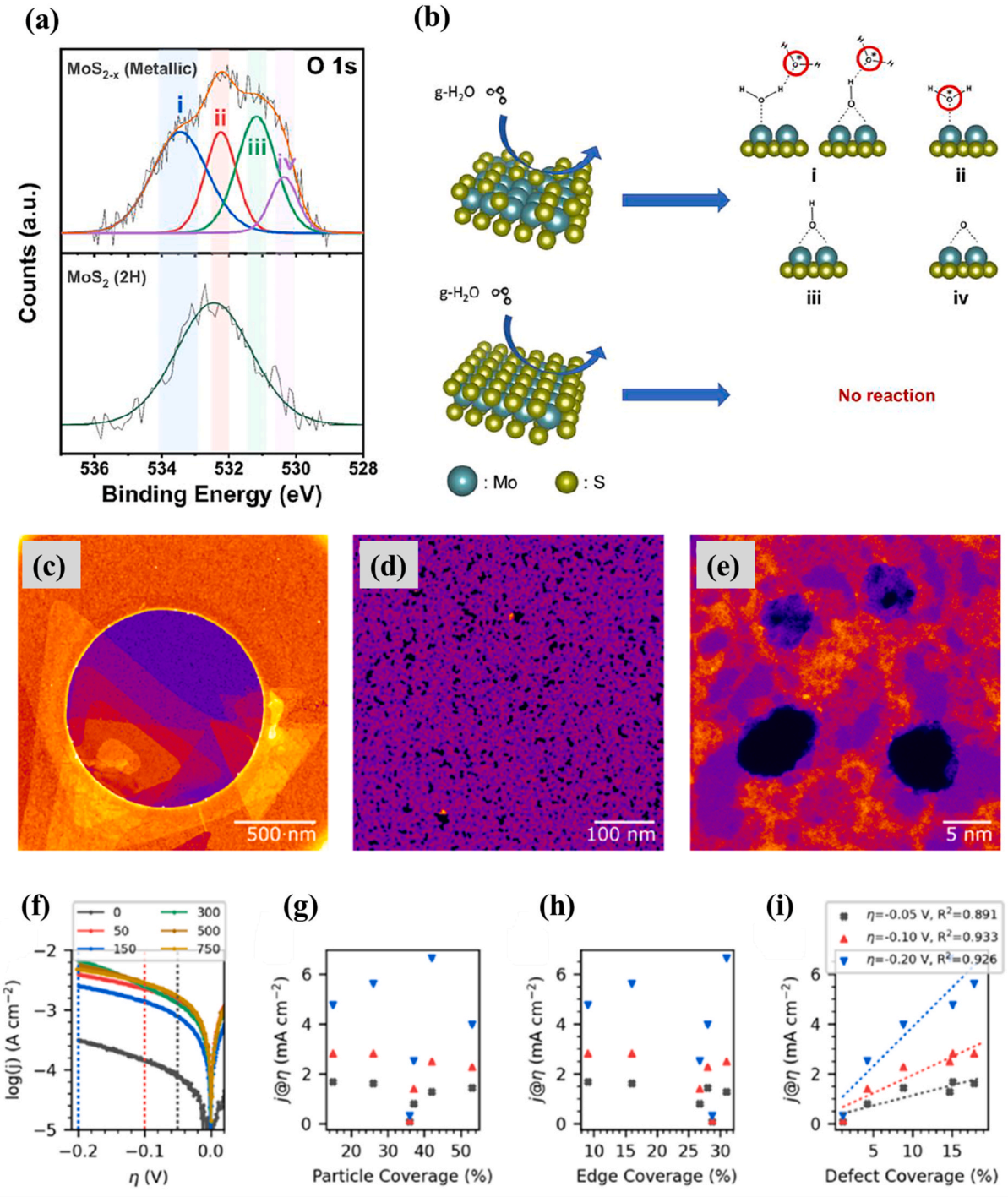

Fig. 5. (a) Comparison of high-resolution O 1s XPS spectra of pristine MoS_2 (2H, bottom panel) and MoS_{2-x} (Metallic, top panel); (b) Schematic illustration of the products of H_2O dissociative adsorption on the surface of pristine MoS_2 (2H, bottom panel) and MoS_{2-x} (Metallic, top panel). Reused with permission from ref. [117] American Chemical Society, Copyright© 2024. STEM-MAADF images of defects created by swift heavy ion irradiation of 2D MoS_2 flakes (c) a TEM-grid hole covered by MoS_2 layers, where lighter colors represent more layers and purple represents MoS_2 monolayers; (d, e) pore-like defects in the MoS_2 after ion irradiation; (f) Semilogarithmic electrocatalytic response acquired using a 5 mV s^{-1} linear sweep in 0.5 M H_2SO_4. Comparison of the selected $j@\eta$ metrics as a function of (g) total MoS_2 surface coverage, (h) MoS_2 edges per surface area, and (i) proportional coverage of MoS_2 regions affected by defects. Reused with permission from ref. [126] American Chemical Society, Copyright© 2025. (For interpretation of the references to color in this figure legend, the reader is referred to the Web version of this article.)

pores through controlled swift heavy ion (SHI) irradiation with $^{129}Xe^{23+}$ ions [126]. STEM-MAADF images (Fig. 5c–e) visually confirm the formation of well-defined pore-like defects within the MoS_2 basal plane, which is particularly noticeable at atomic resolution. These pores, identified as active catalytic sites, significantly enhance the HER performance (Fig. 5f–i), where semilogarithmic electrocatalytic response curves demonstrate a consistent increase in current density with ion fluence, strongly correlating with the proportion of defect-affected areas. Raman spectroscopic mapping revealed a binary classification of regions, either strained with pores or pristine, enabling precise quantification of defect density. The analysis indicates that these basal-plane pores outperform the well-known edge sites as catalytic reaction sites for HER, with electrocatalytic performance aligning closely with the proportion of defect-affected areas rather than total surface coverage or edge-site concentration. This work opens avenues for future scale-up through bulk irradiation followed by exfoliation or the use of highly charged ions, providing a promising pathway for optimizing 2D material-based electrocatalysts.

Xiao et al. investigated the impact of ion energy and plasma density on the HER performance of $MoSe_2$ nanosheets, demonstrating that plasma etching and induced multivacancies enhance catalytic efficiency [127]. A low-pressure capacitively-coupled plasma to modify $MoSe_2$ nanosheets was utilized, revealing that a power of 20 W optimally creates irregular through-holes and defects, achieving a low overpotential of 148 mV at 10 mA cm^{-2} and a Tafel slope of 51.6 mV dec^{-1}. Advanced computational and theoretical analyses provided compelling evidence for the enhanced performance resulting from the observed structural changes. Specifically, plasma simulations and finite element method (FEM) analyses confirmed the beneficial structural modifications: these changes were shown to successfully increase the local electric field and

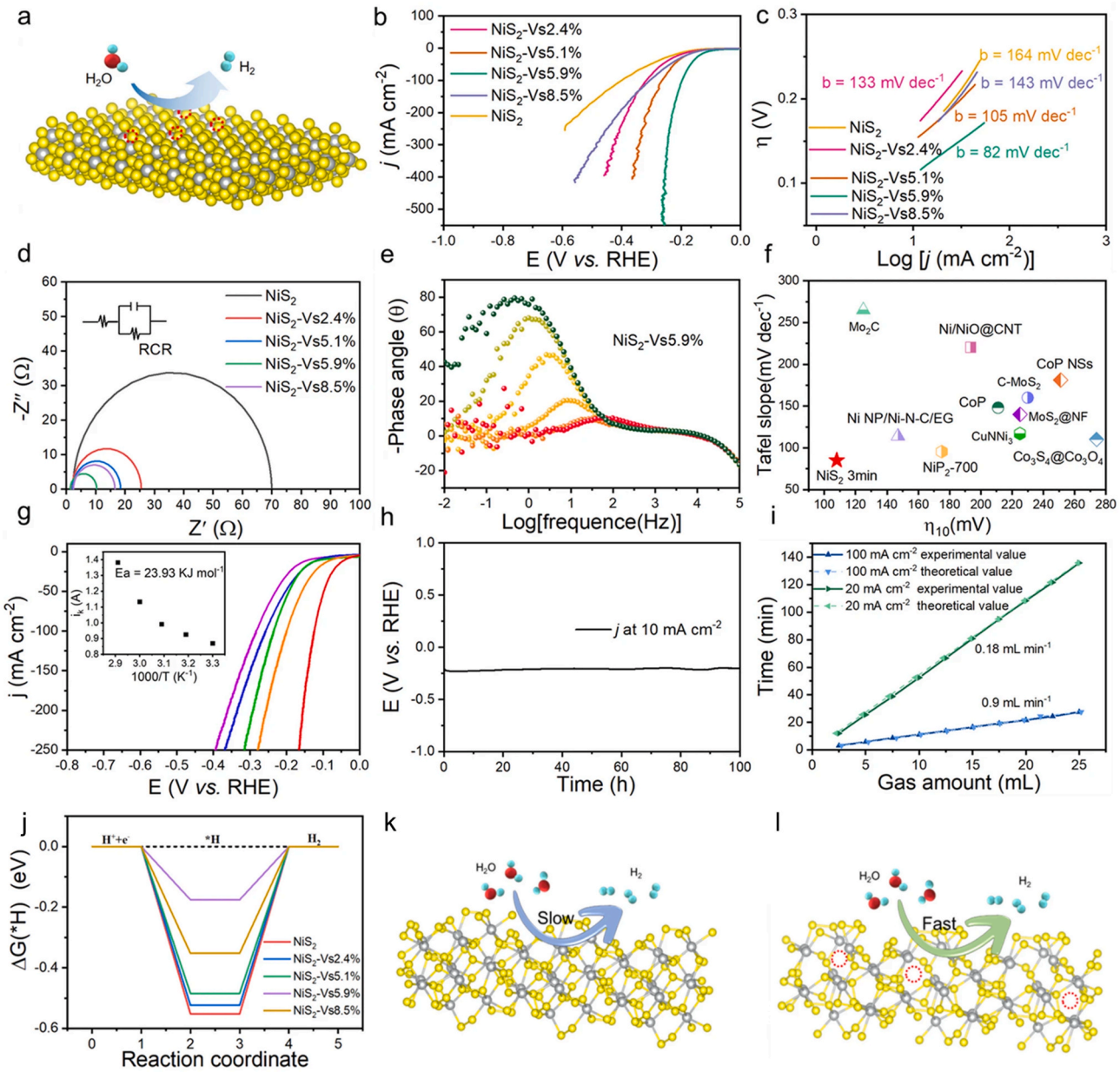

Fig. 6. (a) Schematic diagram of hydrogen evolution of the NiS_2 NSs with S vacancies, (b) LSV curves, (c) Tafel plots and (d) EIS curves of the NiS_2 with varied S vacancies; (e) Bode phase plots of NiS_2-V_s 5.9%; (f) Comparison of both kinetics (Tafel slope) and activity; (g) LSV curves of NiS_2-V_s 5.9% NSs at different temperatures; (h) Chronoamperometric response of NiS_2-V_s 5.9% NSs at 10 mA cm^{-2}; (i) Experimentally and theoretical measured produced H_2 amounts; (j) ΔG_{H^*} of the NiS_2 nanosheets with a series of S vacancies concentrations; (k, l) Scheme of NiS_2 nanosheets catalysts with and without S vacancies. Reproduced from ref. [128] under the terms of the CC-BY Creative Commons Attribution 4.0, Copyright© 2024, The Author(s), published by Springer Nature.

the number of accessible active sites, both critical factors that significantly accelerate electron transfer kinetics. Furthermore, DFT calculations provided a mechanistic understanding at the atomic level, revealing that the presence of selenium vacancies effectively reduced the ΔG for the key reaction steps and simultaneously led to a narrower electronic bandgap. This synergistic effect-increased electric field/active sites and favorable thermodynamic/electronic structure-fully explains the improved catalytic efficiency of the synthesized materials. The study highlights that moderate ion energy and density balance etching and plasma-induced damage, optimizing HER activity, with stability maintained over 10,000 cycles, and provides new insights into plasma functionalization to design high-performance HER.

Jin et al. explore the optimization of NiS_2 nanosheets for the HER using an Ar plasma etching strategy to introduce sulfur vacancies (V_s) as shown in Fig. 6a. Raman and XPS spectra, comparing various NiS_2 phases, including the porous 1T phase, which exhibits distinct vibrational modes and a higher ratio of reduced sulfur species, confirming effective vacancy introduction at the optimal 5.9% concentration (NiS_2-V_s 5.9%) after 3 min of etching for the best LSV performance (Fig. 6b). For the optimized NiS_2-V_s 5.9% nanosheet catalyst, the Tafel slope was measured at 82 mV dec^{-1}. This value reflects the fastest HER kinetics compared with those of NiS_2 (182 mV dec^{-1}), NiS_2-V_s 2.4% (165 mV dec^{-1}), NiS_2-V_s 5.1% (150 mV dec^{-1}), and NiS_2-V_s 8.5% (146 mV dec^{-1}), indicating an efficient charge transfer process as shown in Fig. 6c. This enhanced performance is directly attributed to a dual improvement in the catalyst's structure and electronics, both stemming from the introduction of sulfur vacancies. Specifically, these vacancies led to a notable increase in active sites and an optimized electronic structure. This structural and electronic modification was convincingly confirmed and meticulously visualized through a suite of advanced electron microscopy techniques, including TEM, SAED, and HAADF-STEM analyses. From Fig. 6d–i, the Nyquist plots reveal that NiS_2-V_s 5.9% exhibits the lowest solution resistance and charge-transfer resistance among the compared electrodes, indicating superior charge transfer efficiency. EIS analysis further shows that the phase angle maximum in the Bode plot for NiS_2-V_s 5.9% shifts most rapidly to lower values with changing potential, confirming its fastest HER kinetics, while temperature-dependent studies yield a low apparent activation energy (E_{app}) of 23.9 kJ mol^{-1} at a reduced onset potential, highlighting its excellent activity as well (Fig. 6g). Notably, NiS_2-V_s 5.9% demonstrates state-of-the-art performance among reported alkaline HER catalysts (Fig. 6f) exceptional long-term stability after 100 h at 10 mA cm^{-2} (Fig. 6h), and a high hydrogen evolution rate of 0.9 mL min^{-1} at 100 mA cm^{-2} as measured by the drainage method (Fig. 6i). This structural tailoring enhances H* adsorption, contributing to the observed ultralow onset potential of 68 mV and stability over 100 h in 1 M KOH. In situ attenuated-total-reflection Fourier transform infrared spectroscopy (ATR-FTIRS) confirmed that the S–H* peak at low voltage on NiS_2-V_s 5.9% optimizes H* adsorption, while density functional theory (DFT) calculations supported this with an optimal $|\Delta G_{H^*}|$ of 0.17 eV coupled with the fast kinetics (Fig. 6j-l). These findings exhibit the potential of precise vacancy control to tune the electronic structure of NiS_2, offering a cost-effective and stable alternative to noble-metal catalysts.

Very recently, Guo et al. investigated the impact of sulfur vacancies in a MoS_2/Ni_3S_2 for HER [129]. The researchers utilized a two-step process of solvothermal synthesis and high-temperature pyrolysis to precisely create and tune these defects. This approach resulted in the optimized catalyst, $Ni_3S_2/MoS_2(V_{g10})$, that exhibited a low overpotential of 84 mV at 10 mA cm^{-2} and a Tafel slope of 61.6 mV dec^{-1}. Characterization techniques like XPS and ESR confirmed that the sulfur vacancies modulate the electronic structure, optimizing the hydrogen adsorption energy and promoting efficient charge transfer at the interface. The study also highlighted the long-term stability, with performance remaining excellent over 130 h. This work offers new insights into how defect engineering can be used to design and enhance high-performance, non-precious-metal HER catalysts.

Another modified surface approach is doping to enhance the catalytic activity, which involves the strategic incorporation of foreign atoms into the host material to alter its electronic and structural properties [40,130–132]. This method can optimize the active sites by adjusting the Gibbs free energy of hydrogen adsorption, thereby improving the efficiency of HER. Doping has been shown to increase metallic character, enhance charge transfer, and stabilize metastable phases, leading to lower overpotentials and faster reaction kinetics [133]. Additionally, doping can introduce defects or vacancies that expose more catalytic sites, further boosting performance, as evidenced by recent studies demonstrating significant improvements in HER activity, which is discussed and highlighted in the following part. This versatile technique thus offers a promising avenue for tailoring catalysts to meet industrial demands for sustainable hydrogen production.

Xue et al. explored that the HER performance is significantly enhanced through the strategic doping of Fe into MoS_2 nanostructures [134]. In detail, Fe doping modifies the electronic structure, shifting the Mo 3d binding energies to optimize hydrogen adsorption and reduce overpotentials, with Fe–MoS_2-5 achieving 173 mV at 10 mA cm^{-2} with a Tafel plot of 40.1 mV dec^{-1} in 0.5 M H_2SO_4. This doping effect increases the electrochemically active surface area, as evidenced by a higher double-layer capacitance of 39.8 mF cm^{-2}, facilitating improved charge transfer and reaction kinetics. The incorporation of Fe also induces structural changes, such as nanocanopy formation, which further boosts active site availability and stability over 1000 CV cycles.

Otherwise, Bao's group synthesized mesoporous MoS_2 [135] (mPF-MoS_2) oriented vertical growth of MoS_2 nanosheets around the mesopores to boost the number of active edge sites and fabricated an atomic Co-doping mPF-MoS_2 framework (resulting in mPF-Co-MoS_2) to intrinsically enhance HER activity, which demonstrates excellent durability and a low overpotential of 156 mV at 10 mA cm^{-2} in acidic electrolyte. Density functional theory (DFT) calculations further support these findings, confirming that appropriate Co doping significantly promotes the HER activity. In another study, Liang et al. synthesized the $Ni_{0.05}Mo_{0.95}S_2$ electrocatalyst via a facile one-step electrodeposition method [136], exhibiting high HER performance in acidic solutions, achieving a low overpotential of 215 mV at 10 mA cm^{-2} and a Tafel slope of 62 mV dec^{-1}. The incorporation of 5 at% Ni into 2H–MoS_2 expands the interlayer spacing from 0.63 nm to 0.83 nm, creating abundant active sites and enhancing hydrogen adsorption/desorption kinetics. The Ni–Mo–S structure promotes a Volmer-Heyrovsky mechanism, accelerating HER kinetics due to increased surface defects and improved electrical conductivity. The porous morphology exposes more edge sites, further boosting electrocatalytic activity. Additionally, $Ni_{0.05}Mo_{0.95}S_2$ demonstrates excellent stability, with minimal overpotential increase after 1000 cycles and 12 h in 0.5 M H_2SO_4.

Recently, the HER has been significantly enhanced by the use of Co-doped 1T-MoS_2 microspheres embedded in N-doped reduced graphene oxide (N-rGO), as demonstrated by Gyawali et al. [137], where Co doping increases the number of active sites and stabilizes the metastable 1T phase (Fig. 7a–c). This doping effect modifies the electronic structure, lowering the overpotential to 142 mV at 10 mA cm^{-2} and a Tafel slope of 48 mV dec^{-1} in alkaline media, as the Co atoms form robust Co–S covalent bonds that improve hydrogen adsorption dynamics. The incorporation of Co critically stabilizes the 1T phase of MoS_2, increasing active sites and improving charge transfer kinetics, which are beneficial for HER performance. Compared to commercial Pt/C, which achieves an overpotential of 63 mV, the $Co_{0.18}$/1T-$Mo_{0.82}S_2$@N-rGO shows competitive performance with excellent stability over 24 h at 10 and 100 mA cm^{-2}. The synergistic effect between Co doping and N-rGO is key to optimizing hydrogen adsorption and desorption, as supported by electrochemical impedance spectroscopy results. These doping strategies collectively reduce energy barriers and improve stability, making Co-doped 1T-MoS_2 a promising candidate for efficient HER.

Meanwhile, HER is markedly improved with vanadium (V)-doped MoS_2 electrocatalysts using silicotungstic acid as an electron mediator,

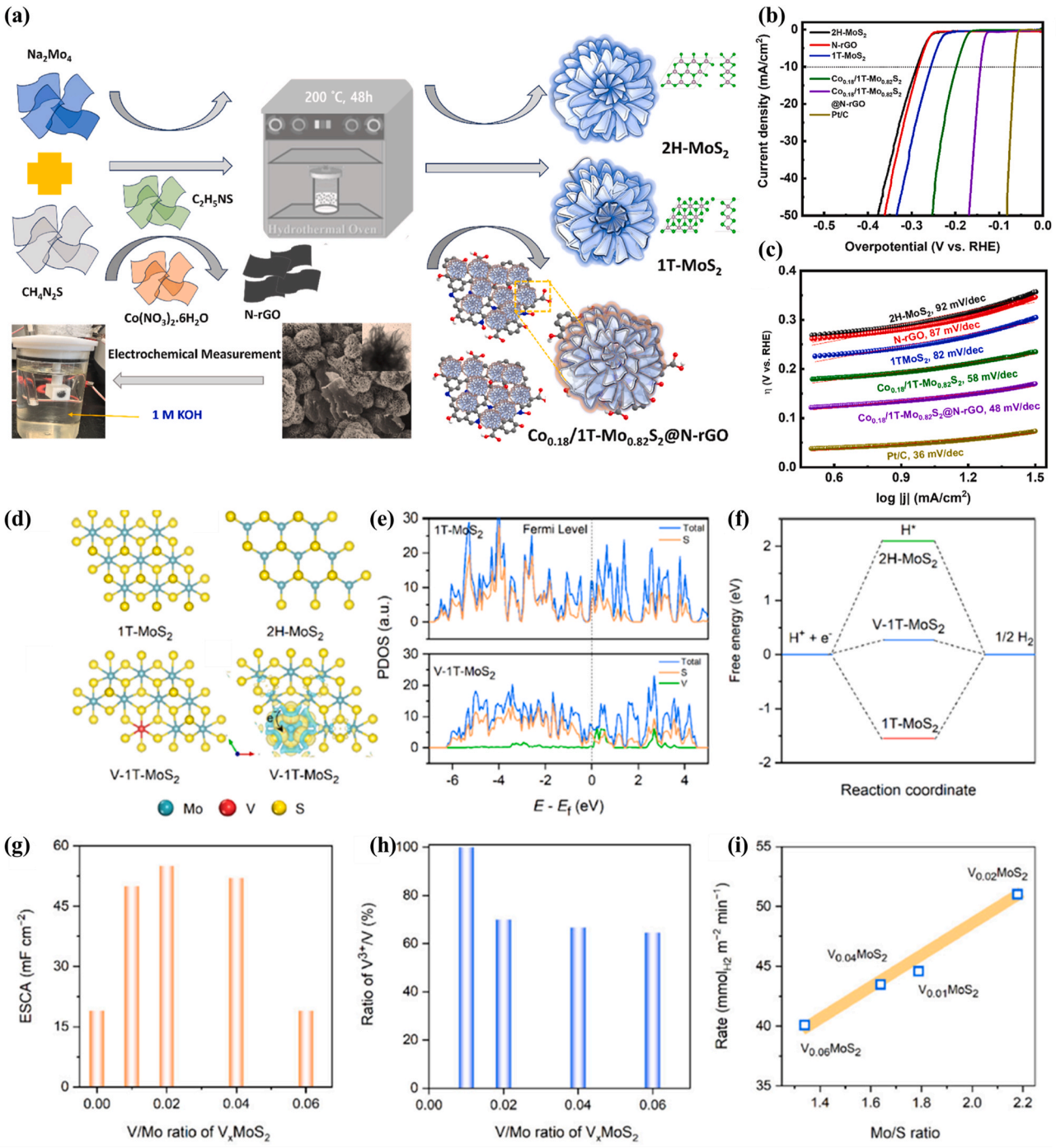

Fig. 7. (a) the overall synthesis process, (b) HER polarization curves, (c) Tafel slopes of N-rGO, 2H–MoS_2, 1T-MoS_2, $Co_{0.18}$/1T-$Mo_{0.82}S_2$, and $Co_{0.18}$/1T-$Mo_{0.82}S_2$@N-rGO samples. Reused with permission from ref. [137] Elsevier, Copyright© 2024. (d) Structural models of 1T-MoS_2, 2H–MoS_2, and V-1T-MoS_2, where cyan and yellow regions indicate electron accumulation and depletion, respectively. (e) PDOS of 1T-MoS_2 and V-1T-MoS_2. (f) Calculated Gibbs free energy diagram for hydrogen adsorption. (g) Effect of the V/Mo ratio on the electrochemically active surface area. (h) Dependence of V/Mo ratio on V^{3+}/V ratio derived from XPS data. (i) Relationship between the normalized HER rate and the Mo/S ratio based on XPS results. Reused with permission from ref. [133] American Chemical Society, Copyright© 2025. (For interpretation of the references to color in this figure legend, the reader is referred to the Web version of this article.)

as demonstrated very recently by Zheng et al. [133]. This nanocomposite achieves a significantly lower overpotential, enhancing the HER rate to 696.4 mmol H_2 g^{-1} min^{-1} compared to 140.7 mmol H_2 g^{-1} min^{-1} for pristine MoS_2, driven by accelerated proton adsorption and transfer kinetics. The mechanism follows a Volmer-Heyrovsky pathway, with Tafel plots showing a reduced slope of 95 mV dec^{-1} for $V_{0.02}MoS_2$, indicating improved rate-limiting steps compared to 182 mV dec^{-1} for MoS_2, where the Volmer step (proton adsorption) is enhanced by V doping, followed by the Heyrovsky step. DFT calculations (Fig. 7d–i) reveal that V doping shifts the Gibbs free energy of hydrogen adsorption (ΔG_{H^*}) on sulfur sites from −1.6 eV in 1T-MoS_2 to 0.3 eV in V-1T-MoS_2, approaching the thermoneutral value, while electron delocalization from S to V sites - optimizes proton transfer to adjacent Mo/V sites. V doping introduces defect sites and modulates the electronic structure, increasing active site availability, while silicotungstic acid facilitates inner-sphere electron transfer, enhancing overall kinetics. Stability is

confirmed with $V_{0.02}MoS_2$ retaining its morphology and performance over multiple tests, positioning it as a viable Pt alternative. This approach highlights a promising strategy for efficient and stable HER catalysis.

In another study, the Chu's group designed the 1T-MoS_2-Pt catalyst, with 14.3 wt% Pt nanoparticles confined within metallic 1T-MoS_2 nanosheets, which exhibits exceptional HER performance in simulated seawater [138], achieving an ultralow onset potential of 65.6 mV vs RHE and an overpotential of 123 mV to achieve a current density of 10 mA cm^{-2} in simulated seawater (1.0 M KOH + 0.5 M NaCl) and a Tafel slope of 64 mV dec^{-1}, rivaling the 40 wt% Pt/C commercial catalyst. The metallic 1T-MoS_2 phase plays a critical role, serving as a robust reducing agent, enabling in-situ reduction of Pt^{4+} into zero-valence Pt fine and small nanoparticles (average 2.35 nm) without additives, while its enlarged interlayer spacing (~0.9 nm) and abundant defects facilitate Pt diffusion, anchoring, and confinement at edges, steps, and vacancies. Significantly, this space-confinement effect prevents Pt aggregation and especially corrosion from aggressive Cl^- ions in seawater, maintaining particle size stability (minor increase to ~ 3.32 nm post-HER) and sustained activity over 12 h at a current density of 10 mA cm^{-2}. The high electrical conductivity and active 1T phase accelerate charge transfer and the H* adsorption/desorption, mitigating kinetic barriers in alkaline-chloride environments. The in-situ growth on graphite paper ensures seamless interfacial contact, reducing resistance and enhancing durability against seawater's corrosive impurities. Overall, the 1T-MoS_2 framework synergistically integrates reduction capability, structural confinement of ultrafine Pt, and electronic tuning to deliver cost-effective, corrosion-resistant seawater splitting.

Phosphorus (P) doping for $MoSe_2$ is also considered a promising approach to significantly enhance HER performance, as demonstrated by Zhang et al. [139], which optimizes the atomic hydrogen binding energy under high coverage conditions. Self-standing P-doped $MoSe_2$ nanosheets grown on carbon fiber paper (P-doped $MoSe_2$/CFP) exhibit a reduced overpotential of 186 mV at 50 mA cm^{-2}, a marked improvement over the 237 mV required by undoped $MoSe_2$/CFP, due to the inhibition of nanosheet aggregation and exposure of numerous active sites. The introduction of P atoms into the $MoSe_2$ lattice lowers the Gibbs free energy of hydrogen adsorption (ΔG_{H^*}) to 0.202 eV at 75% hydrogen coverage, compared to 0.296 eV at 25% for undoped $MoSe_2$, facilitating easier adsorption and desorption processes. This doping effect also reduces the Tafel slope to 54.3 mV dec^{-1}, indicating faster HER kinetics via a Volmer-Heyrovsky mechanism, and enhances the formation of adsorbed hydrogen species during the Volmer reaction. The hierarchical 3D structure of P-doped $MoSe_2$/CFP, supported by conductive CFP, further improves electron transfer efficiency and charge kinetics.

Otherwise, the (Mo, N)–$NiSe_2$/NF nanosheets reported by Gao et al. [140] optimize the active sites by fine-tuning the hydrogen adsorption free energy (ΔG_{H^*}), thereby improving the HER efficiency. In detail, Mo doping increases the specific surface area from 28.5 m^2 g^{-1} for pure $NiSe_2$ to 54.3 m^2 g^{-1} for Mo–$NiSe_2$/NF by altering the morphology of $NiSe_2$ nanosheets into a disordered, petal-like structure, thus exposing additional reactive sites. Nitrogen doping, also detailed in their study, accelerates intrinsic reaction kinetics and introduces new catalytic centers through strong electronic interactions, as evidenced by a positive shift in the Ni 2p binding energy by approximately 0.3 eV in XPS analysis. The synergistic effect of this anion-cation dual-doping results in a porous structure with a high electrochemical double-layer capacitance (C_{dl}) of 90.5 mF cm^{-2} and a low overpotential of 82 mV at 10 mA cm^{-2}, surpassing many reported transition metal selenides, while the Tafel slope decreases to 84.5 mV dec^{-1}, indicating faster HER kinetics via a Volmer-Heyrovsky mechanism with the Volmer step as the rate-limiting process, as confirmed by the Tafel analysis in their work. This method highlights doping as a versatile and promising technique for developing cost-effective, high-performance electrocatalysts for sustainable hydrogen production.

To summarize, these defect and doping strategies are highly effective, complementary approaches for enhancing HER in TMS/TMSe catalysts. Vacancies - introduced via plasma, ion irradiation, or controlled synthesis - create extra active sites, activate basal planes, lower ΔG_{H^*}, reduce water dissociation barriers, and improve conductivity, leading to ultralow overpotentials and Tafel slopes. Doping with heteroatoms (Fe, Co, Ni, V, Mo, N, P) primarily tunes electronic structure, shifts d-band centers, narrows bandgaps, stabilizes metallic phases (e.g., 1T-MoS_2), and optimizes ΔG_{H^*} under high coverage, yielding excellent kinetics and durability. Vacancies excel at boosting extrinsic site density and basal-plane activity, while doping dominates intrinsic electronic modulation and phase stabilization. The strongest performers integrate both strategies for synergistic site creation, charge transfer, and long-term stability (>100 h or >10,000 cycles). These design rules provide clear, scalable pathways to noble-metal-free HER catalysts, with future emphasis on precise defect/dopant control and real-world electrolyte tolerance. On the other hand, although defect engineering introduces vacancies to create active sites and lower energy barriers, boosting kinetics in acidic/alkaline media, yet excessive defects risk lattice instability or reduced mechanical integrity, requiring precise control to avoid performance degradation over extended cycles. Also, doping finely tunes electronic structures for optimized ΔG_{H^*} and phase stabilization, enhancing intrinsic activity, but it may introduce foreign elements that complicate material uniformity or increase costs without always guaranteeing proportional stability gains.

3.3. *Interface-driven heterostructure engineering*

Heterostructures are engineered to form interfaces between distinct phases, where the core HER enhancement originates directly from the heterointerface through rapid interfacial charge transfer, elevated local electron density, creation of new active sites at the junction, and precise modulation of surface electronic structure to drive ΔG_{H^*} toward the ideal near-zero value essential for optimal catalysis [141,142]. Beyond electronic effects, heterostructure engineering frequently enables improved electrochemical stability, enhanced mass transport, and the formation of advanced morphologies (e.g., hollow, core-shell, or layered architectures) that further amplify catalytic centers and deliver superior long-term HER efficiency and durability [143–145].

Xie et al. synthesized a novel electrocatalyst by directly coating a graphdiyne (GDY) nanowall onto CoS_2 nanowire arrays [146]. This in-situ growth technique achieved a precise interface where the 2D (211) plane of CoS_2 directly aligns with the GDY plane. This structural configuration was meticulously confirmed through various characterization methods, including SEM images of the GDY/CoS_2/CC composite, HRTEM images detailing the GDY/CoS_2 nanowire, and STEM elemental mapping for Co, S, and C within the nanowire (Fig. 8a–h). This unique heterojunction design provides significant catalytic synergy by increasing the availability of active sites from both the GDY carbon atoms and CoS_2 planar unsaturated sulfur. Crucially, the electron-rich nature of the GDY component further facilitates efficient electron transfer across the two-phase interface, thereby markedly enhancing the combined catalytic effect of the heterostructure. Their optimized electrocatalyst demonstrated exceptional performance, exhibiting a low overpotential of 97 mV at 10 mA cm^{-2}, a high catalytic current density, and a small Tafel slope of 56 mV dec^{-1}. This superior performance is attributed to the optimized heterojunction, which not only provides abundant active sites but also significantly boosts electronic conductivity. Furthermore, the catalyst maintained remarkable stability for up to 36 h, a crucial characteristic for practical applications. In another study, Poudel et al. developed a Mo_3Se_4–NiSe core-shell nanowire array on nickel foam via a single-step hydrothermal process, offering a low-cost, efficient electrocatalyst in alkaline and natural seawater [147]. The heterostructure exhibits low overpotentials of 84.4 mV in alkaline and 166 mV in seawater at 10 mA cm^{-2}. Tafel slopes of 59.62 mV dec^{-1} in alkaline and 90.12 mV dec^{-1} in seawater indicate fast HER kinetics, following a Volmer-Heyrovsky mechanism with

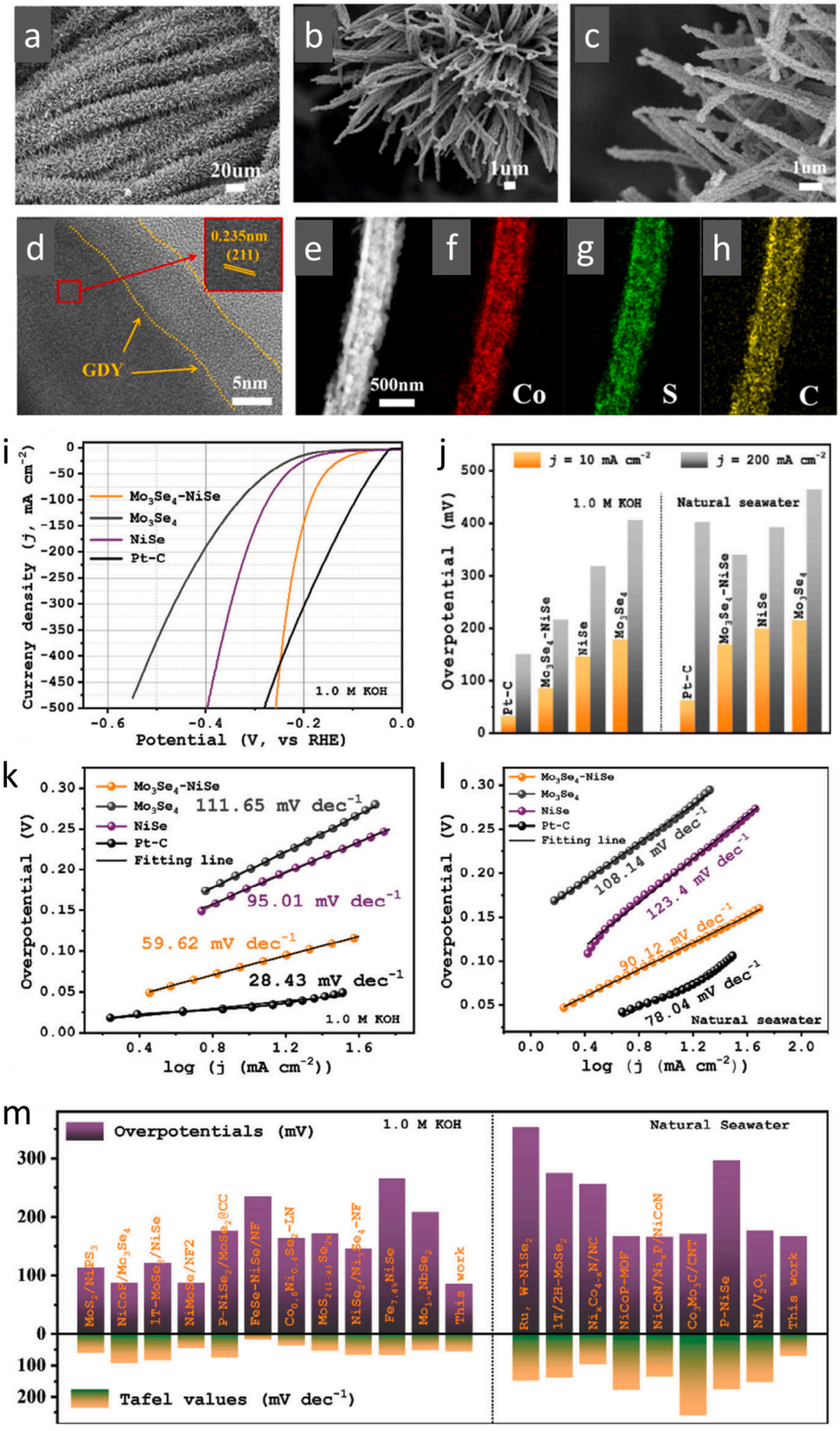

Fig. 8. (a-c) SEM images of GDY/CoS_2/CC. (d) HRTEM images of GDY/CoS_2 nanowire. (e-h) The STEM elemental mapping of Co, S, C for the GDY/CoS_2 nanowire. Reused with permission from ref. [146] Elsevier, Copyright© 2021. (i) HER polarization curves of Mo_3Se_4–NiSe, Mo_3Se_4, NiSe, and Pt–C, (j) HER overpotentials for all electrocatalysts at different current densities, (k-l) Tafel plots from the early stages of HER polarizations, (m) Comparison of a series of Ni- and Mo-based electrocatalysts for H_2 production. Reused with permission from ref. [147] Wiley-VCH, Copyright© 2024.

electro-desorption as the rate-limiting step, surpassing many Ni- and Mo-based catalysts (Fig. 8i-m). The mechanism involves synergistic electron transfer, with NiSe promoting water dissociation and Mo_3Se_4 enhancing H_2 desorption, supported by DFT calculations showing a ΔG_{H^*} of 0.207 eV at Se active sites. The heterostructure's core-shell design, confirmed by TEM and XRD, increases active site exposure and conductivity due to the rough Mo_3Se_4 shell over the NiSe core. Stability tests demonstrate minimal degradation over 50 h, with the interface maintaining structural integrity. The approach avoids complex multi-step synthesis, using in situ etching and reduction to form the nanowire arrays and offers a scalable route for PGM-free HER catalysts, with potential for broader TMD heterostructure applications.

Zhao et al. developed the $CoSe_2/MoSe_2$ heterostructures [148], enhancing alkaline HER activity by integrating $CoSe_2$ quantum dots onto $MoSe_2$ nanosheets, leveraging the superior water adsorption and dissociation capabilities of $CoSe_2$. Synthesized through a facile refluxing process followed by annealing in argon, these heterostructures, particularly the $0.2CoSe_2/MoSe_2$ composition, achieve an optimal overpotential of 218 mV at a current density of 10 mA cm^{-2} in 1 M KOH, outperforming bare $MoSe_2$ by over 100 mV. The Tafel slope for $0.2CoSe_2/MoSe_2$ reduces to 76 mV dec^{-1}, indicating improved kinetics through a Volmer-Heyrovsky mechanism, compared to 137 mV dec^{-1} for $MoSe_2$, where water dissociation is the rate-limiting step. Detailed electrochemical analyses, including a TOF of 232 s^{-1} at 300 mV for $0.2CoSe_2/MoSe_2$, highlight the synergistic effect where $CoSe_2$ accelerates water dissociation, while $MoSe_2$ facilitates hydrogen adsorption and combination. In another study, Basu developed $NiCo_2S_4/Co_9S_8$ nanotube heterostructures as an efficient catalyst in 1.0 M KOH, synthesized via a hydrothermal method [149]. The heterostructure exhibits a low overpotential of 172 mV to achieve a current density of 10 mA cm^{-2}, outperforming bare Co_9S_8 (293 mV) and $NiCo_2S_4$ (239 mV). The enhanced catalytic activity is attributed to improved charge transportation due to the nanotube morphology and heterostructure formation. Tafel slope analysis revealed a value of 115 mV dec^{-1} for $NiCo_2S_4/Co_9S_8$ nanotube, indicating faster HER kinetics. The material demonstrated stability with an unaltered current density of 100 mA cm^{-2} for 12 h.

Recently, Pratheeksha M et al. reported the conversion of NiMo layered double hydroxide (NiMo LDH) into Mo-doped nickel selenide ($Mo@NiSe_2$) using a simple solvothermal technique [150]. This structural alteration significantly enhances HER catalytic performance, with $Mo@NiSe_2$ achieving an overpotential of 118 mV at 10 mA cm^{-2}, representing a substantial improvement over the 602 mV required by unmodified NiMo LDH. The enhanced activity stems from an optimized d-band electronic configuration, which boosts electron conductivity and increases the surface area, thereby providing more active sites for catalysis. DFT calculations confirm this with a near-zero ΔG_H value of 0.02 eV for $Mo@NiSe_2$, supporting its superior HER efficiency.

Remarkably, a self-supported $NiSe_2$–$RuSe_2$/NF heterostructure catalyst was synthesized recently by Qi et al. [151], demonstrating

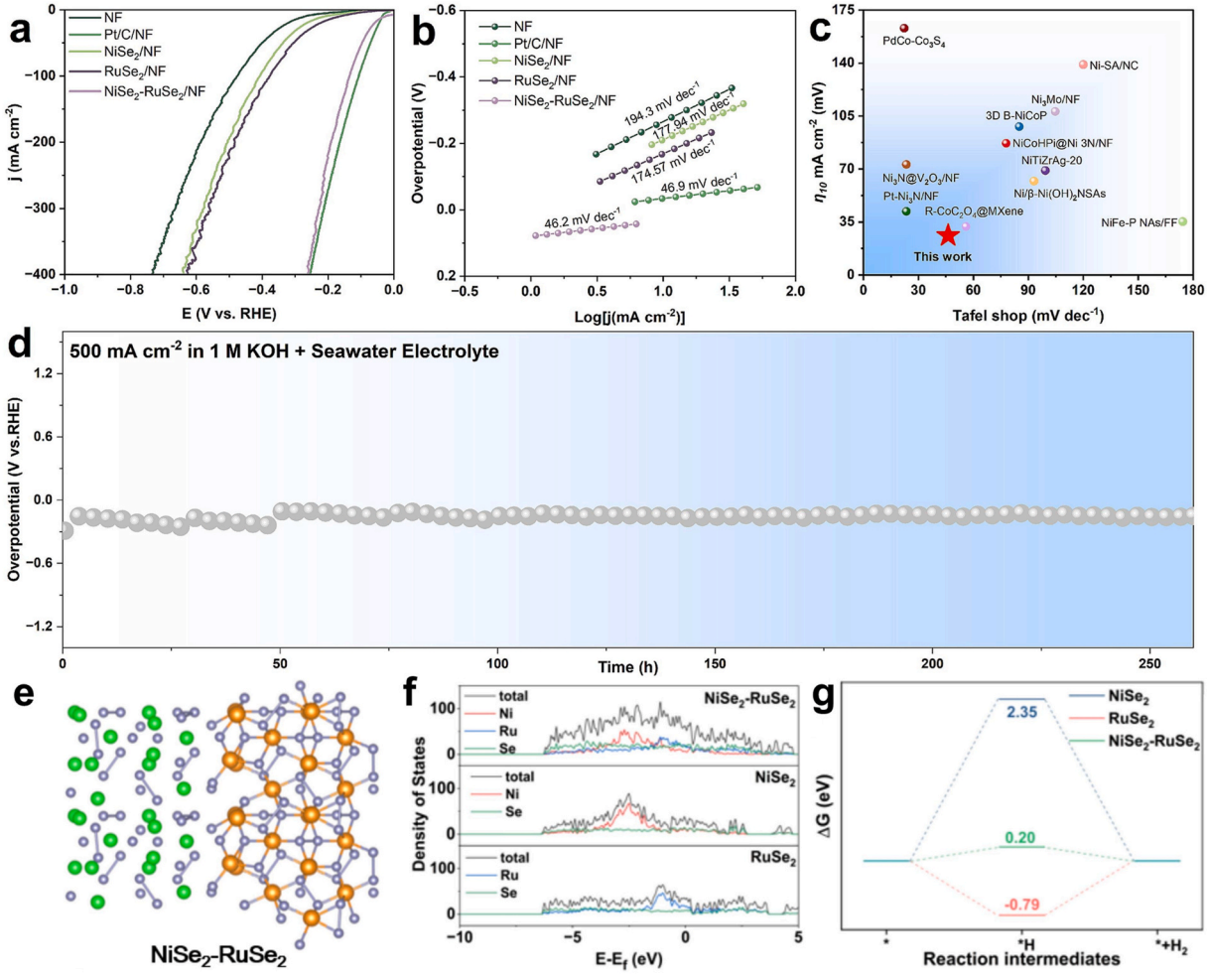

Fig. 9. HER performance in a 1 M KOH + natural seawater solution. (a) The LSV, (b) The Tafel plots, (c) Compares the Tafel slopes and overpotentials at 10 mA cm^{-2}, (d) Long-term stability testing at 500 mA cm^{-2}. (g) LSV curves (scan rate of 5 mV s^{-1}), (e) Atomic models of the optimized configurations for $NiSe_2$–$RuSe_2$ heterojunction, (f) Projected density of states (PDOS) for the $NiSe_2$–$RuSe_2$ heterojunction, $NiSe_2$, and $RuSe_2$, (g) Calculated ΔG_{H^*} at different catalysts. Reused with permission from ref. [151] Elsevier, Copyright© 2025.

exceptional HER performance in a 1 M KOH solution mixed with natural seawater, as shown in Fig. 9a–c. In this environment, $NiSe_2$–$RuSe_2$/NF exhibited the lowest overpotential of 26 mV to achieve a current density of 10 mA cm^{-2}, significantly outperforming the bare nickel foam (NF) at 272 mV, $NiSe_2$/NF at 211 mV, $RuSe_2$/NF at 204 mV, and even the benchmark commercial Pt/C on nickel foam (Pt/C/NF) at 36 mV as depicted in the polarization LSV curves. This ultralow overpotential highlights the catalyst's superior efficiency, requiring minimal energy input to drive the hydrogen evolution process compared to its counterparts. The Tafel slope, a key indicator of HER kinetics, was measured at 46.20 mV dec^{-1} for $NiSe_2$–$RuSe_2$/NF, slightly better than Pt/C/NF at 46.90 mV dec^{-1}, and markedly lower than $NiSe_2$/NF at 177.49 mV dec^{-1} and $RuSe_2$/NF at 174.57 mV dec^{-1}, as shown in the Tafel plots. This reduced Tafel slope reflects faster reaction kinetics, suggesting that the Volmer-Heyrovsky or Volmer-Tafel mechanism is efficiently catalyzed, with the heterojunction enabling a smoother transition of reaction intermediates. The intense electron interactions within the $NiSe_2$–$RuSe_2$/NF heterojunction play a pivotal role, optimizing the electronic structure to enhance H* adsorption energy and facilitate the Tafel step. This catalyst also excels in seawater electrolysis, maintaining stability for over 250 h at a high current density of 500 mA cm^{-2}, surpassing the performance of traditional Pt/C catalysts (Fig. 9d). The enhanced catalytic activity in alkaline and seawater conditions arises from the robust electronic interactions within the bimetallic selenide heterojunction, which optimizes the adsorption and desorption of hydrogen intermediates. This electronic modulation, supported by DFT calculations (Fig. 9e–g) showing a favorable ΔG_{H^*} value close to 0 eV, facilitates faster reaction kinetics and increases the availability of active sites.

Noticeably, this bimetallic selenide heterostructure exhibits exceptional performance in seawater electrolysis by addressing critical challenges. Cl^- oxidation, which competes with HER and risks catalyst corrosion via chlorine gas formation, and sluggish HER kinetics are mitigated by the heterostructure's strong electronic interactions, optimizing ΔG_{H^*} (~0.2 eV) for selective HER kinetics. Mg^{2+} and Ca^{2+} precipitation, which clogs electrode surfaces, is minimized by the catalyst's 3D porous structure, enhancing mass transport and resisting scaling, as confirmed by EDS mapping showing no Mg/Ca deposits after 250 h of operation. Seawater's buffering capacity creates pH gradients that hinder proton availability, but the heterostructure's design promotes efficient mass transfer and rapid bubble desorption, sustaining low overpotentials during seawater electrolysis. Its in-situ growth on conductive nickel foam enhances charge transfer and prevents delamination of active sites, and serves as a protective coating, shielding the catalyst from Cl^--induced corrosion and ensuring long-term stability in harsh seawater conditions, ensuring stability over 250 h at 500 mA cm^{-2}. Overall, the synergy of material design and electronic tuning positions $NiSe_2$–$RuSe_2$/NF as a promising solution for advancing renewable energy technologies in challenging electrolytic conditions.

Li et al. reported the development of NiS/$NiSe_2$ heterostructures, synthesized through a one-pot hydrothermal method [152], with Ni_4–Se_2–S_2 demonstrating outstanding HER performance in 1 M KOH. This catalyst achieves a low overpotential of 155 mV at 10 mA cm^{-2}, surpassing many transition metal-based alternatives and closely approaching the performance of noble metal catalyst Pt/C. The Tafel slope of 101 mV/dec reflects rapid HER kinetics, attributed to the synergistic electronic interactions at the NiS–$NiSe_2$ interface, which enhance charge transfer and increase active site availability. Stability tests show no significant current drop after 86,400 s at the specified overpotential, underscoring its durability. The high performance is driven by the optimized NiS-to-$NiSe_2$ ratio (5.82/2.47), which balances conductivity and surface area, while DFT calculations reveal a downshifted d-band center that lowers energy barriers, boosting catalytic efficiency for HER.

Rehman et al. recently developed a novel 1T-WS_2/1T-WSe_2 heterostructure using a low-temperature plasma-assisted chemical vapor reaction (PACVR), specifically through plasma-assisted sulfurization and selenization, to enhance HER performance [153]. The heterostructure exhibits a low Tafel slope of 57 mV dec^{-1} and an overpotential of 291 mV at 10 mA cm^{-2} in 0.5 M H_2SO_4, attributed to the metallic 1T phase and synergistic electron transfer from WS_2 to WSe_2 at the interface. Plasma treatment increases surface roughness, boosting active site exposure, while the process maintains stability over 5000 cycles and 24 h, as confirmed by polarization and chronoamperometry tests. The study utilized advanced characterization techniques like Raman spectroscopy, XPS, and TEM to validate the heterostructure's composition and morphology, showing a 20 nm film thickness with a 1T phase dominance. Compared to pure WS_2 and WSe_2, the heterostructure demonstrates superior electrocatalytic activity, with a higher ECSA of 151.1 cm^2 and a TOF of 2.7 s^{-1} at 300 mV overpotential. This approach offers a scalable, cost-effective method for synthesizing efficient HER catalysts, addressing challenges with traditional high-temperature methods like CVD.

In another research, Liu et al. (2024) synthesized a MoS_2@o-$CoSe_2$ heterostructure derived from Co-based metal organic framework (Co-MOF) for efficient HER [154] in 1 M KOH, achieving a low overpotential of 34 mV at 10 mA cm^{-2} and a Tafel slope of 41 mV dec^{-1}. The heterostructure outperforms commercial Pt/C at high current densities, attributed to its porous ultrathin nanosheet morphology and synergistic effects from the tightly bonded interface. The phase transition to orthorhombic *o*-$CoSe_2$, facilitated by sulfur content during selenization, enhances electron transport and reduces the Gibbs free energy of hydrogen adsorption. TEM and XPS analyses confirm the heterostructure's composition, with a tightly bonded MoS_2-*o*-$CoSe_2$ interface exposing abundant active sites. The mechanism involves water dissociation on MOF nanosheets followed by H_{ads} migration to interface edges, accelerating the Heyrovsky step. DFT calculations show a lower ΔG_{H^*} (0.34 eV) for MoS_2@o-$CoSe_2$ compared to MoS_2@c-$CoSe_2$, supporting its superior HER activity. The catalyst maintains stability over 72 h with negligible current decay, and its large ECSA further boosts performance. This approach highlights phase engineering and MOF-derived heterostructures as a scalable strategy for noble-metal-free HER catalysts.

Taken together, heterostructure engineering excels by forming intimate interfaces between distinct phases, where the primary boost to HER performance stems from direct interfacial charge transfer, electronic reconfiguration, and synergistic active-site creation at the boundary. This approach optimizes ΔG_{H^*} near zero, accelerates reaction kinetics (often Volmer-Heyrovsky), and enhances water dissociation or H* desorption through complementary roles of each phase. Core-shell, quantum-dot-on-nanosheet, bimetallic selenide, and plane-aligned designs consistently deliver ultralow overpotentials and Tafel slope, with exceptional stability in alkaline, seawater, or high-current conditions. Heterostructures stand out for their ability to generate built-in electric fields and electronic synergy at the interface, outperforming single-phase materials in intrinsic activity. The key design rule is that the heterointerface itself acts as the catalytic hotspot, making this strategy ideal for noble-metal-free catalysts targeting challenging electrolytes. Overall, heterostructure engineering provides a powerful pathway for electronic tuning and long-term durability in practical HER applications, but their precise interface designs can trade off scalability for the added complexity of multi-phase synthesis.

3.4. Conductive matrix nanocomposites

Nanocomposites are created through a widely adopted strategy that integrates TMS- or TMSe-based catalysts with other materials, particularly highly conductive carbon-based nanomaterials [34,59,155–158] such as graphene, carbon nanotubes, carbon fibers, activated carbon, or another specialized material like MXene [159]. In detail, carbon-based materials stand out as excellent substrates for composite electrocatalysts owing to their superior electrical conductivity, substantial specific surface area, and robust structural stability. These supports

significantly enhance the uniform dispersion of active sites, accelerate charge transfer, and effectively shield deposited metal particles from corrosion and oxidation in harsh acidic or alkaline electrolytes. Hybridization with such matrices also suppresses particle aggregation, thereby preserving the mechanical integrity of the electrode. As a result, optimization efforts for these composites center on strategies like maximizing active site exposure, further boosting overall conductivity, enlarging accessible surface area, and integrating self-supporting architectures to achieve superior electrochemical performance [160,161]. Achieving these optimizations significantly improves electrical conductivity, enhances structural stability, and ensures better dispersion of active sites, ultimately creating powerful synergistic effects that dramatically boost the overall electrochemical performance of the final catalyst.

Nie et al. developed a well-ordered Co-1T-MoS_2/C superlattice heterostructure using a colloidal synthesis strategy, featuring alternating layers of single-atomic Co-anchored 1T-MoS_2 and carbon nanosheets, as illustrated in Fig. 10 [162]. In detail, the Co-1T-Mo S_2/C superlattice

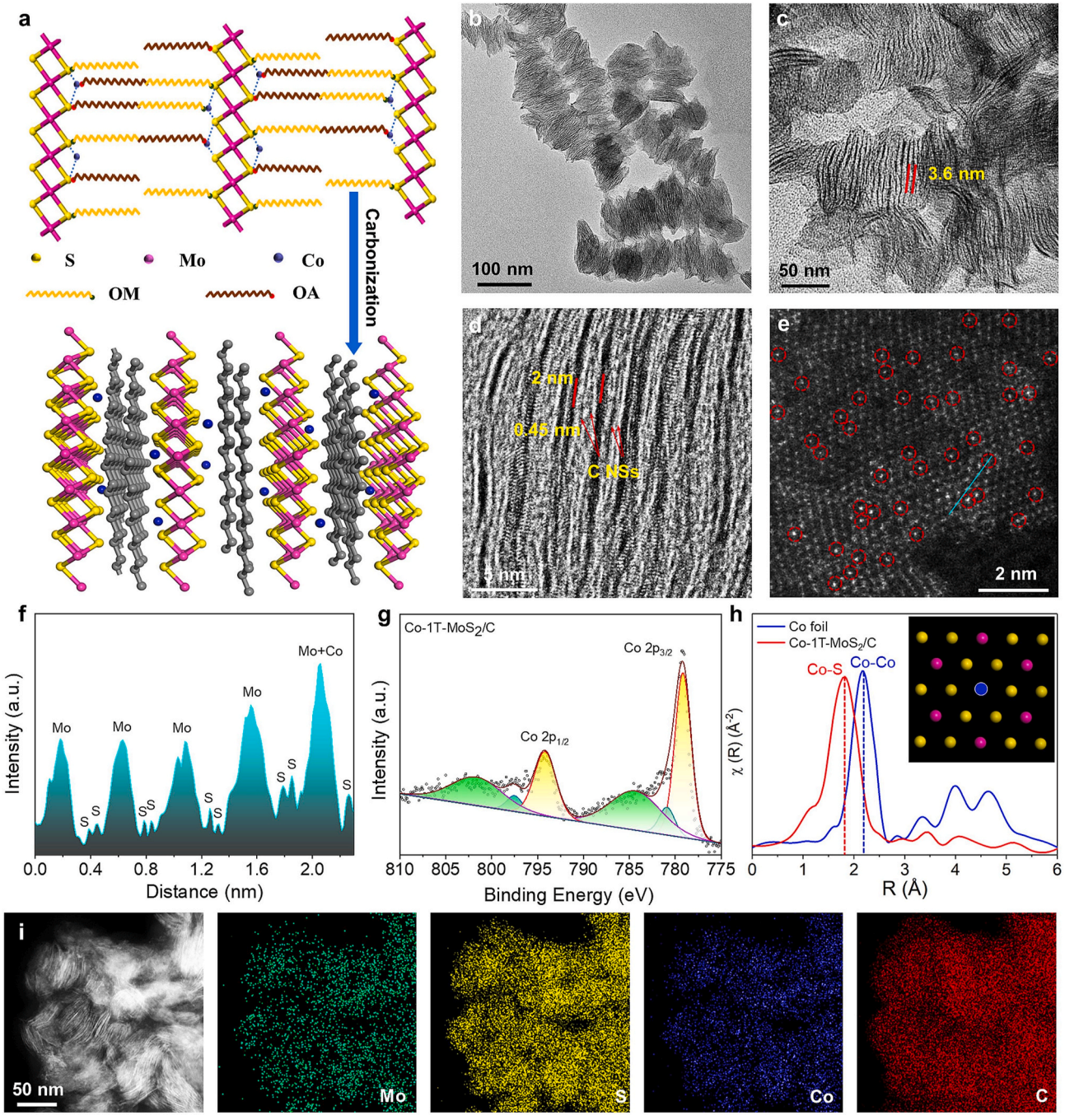

Fig. 10. (a) Crystal structure of Co-1T-MoS_2 (up) and Co-1T-MoS_2/C (down). TEM images of Co-1T-MoS_2 at (b) low- and (c) high-magnification. (d) HRTEM image of the side view of Co-1T-MoS_2/C. (e) HAADF-STEM image of the basal plane of Co-1T-MoS_2/C and (f) the corresponding intensity line profile taken along the line declared in (e). (g) Co 2p XPS spectra of Co-1T-MoS_2/C. (h) EXAFS spectra of Co K-edge for Co-1T-MoS_2/C and reference cobalt foil. The inset displays the atomic model of Co-1T-MoS_2/C, where the yellow, blue, and magenta spheres represent S, Co, and Mo atoms, respectively. (i) HAADF-STEM image of Co-1T-MoS_2/C and corresponding elemental mapping of Mo, S, Co, and C. Reused with permission from ref. [162] Elsevier, Copyright© 2023. (For interpretation of the references to color in this figure legend, the reader is referred to the Web version of this article.)

heterostructure is formed by in situ carbonization of oleylamine (OM) and oleic acid (OA) molecules that were pre-adsorbed on both sides of Co-1T-MoS_2 nanosheets, which transform into ultra-thin carbon nanosheets (C NSs) that separate adjacent MoS_2 monolayers, resulting in an alternating arrangement of Co-1T- MoS_2 and C layers with a well-ordered molecular-level superlattice (Fig. 10a–d). Cross-sectional HRTEM imaging confirms an interlayer spacing of 2.0 nm for the MoS_2 nanosheets, with double C NSs (layer spacing 0.45 nm) sandwiched in between, while FT-IR spectroscopy verifies the successful carbonization through the disappearance of OM and OA characteristic peaks, and XRD patterns match the simulated 1T- MoS_2 structure with a reduced overall layer spacing compared to the precursor Co-1T- MoS_2 nanochains. This synthesis strategy not only generated the carbon nanosheets in situ but also preserved the 1T phase of MoS_2 while introducing atomically dispersed Co atoms onto the basal plane, as confirmed by aberration-corrected HAADF-STEM imaging showing isolated Co atoms (marked in red) randomly distributed above Mo sites (Fig. 10e and f). XPS and EXAFS analyses (Fig. 10g and h) further demonstrate that isolated Co atoms are coordinated with three adjacent S atoms via Co–S bonds while elemental mapping (Fig. 10i) shows uniform distribution of Mo, S, Co, and C throughout the ordered superlattice heterostructure. The structure exhibits high phase stability of the metastable 1T-MoS_2 phase, enhanced by cobalt atoms forming strong Co–S covalent bonds, which stabilize the 1T phase over the 2H phase. Overpotential in 1.0 M KOH is significantly reduced, with Co-1T-MoS_2/C requiring only 135 mV for HER at 10 mA cm^{-2}, outperforming pure 1T-MoS_2 and 2H–MoS_2. Tafel slopes are notably low, at 88.3 mV dec^{-1} for HER, indicating fast reaction kinetics. The mechanism involves synergistic effects between 1T-MoS_2 and carbon nanosheets, with cobalt atoms tuning the electronic structure and creating additional active sites. Sulfur vacancies and N, S dual-doped carbon enhance water adsorption and dissociation, while rapid interfacial charge transfer boosts electrocatalytic performance. The heterostructure's durability is demonstrated by stable operation over 60 h and 1000 CV cycles. DFT calculations confirm the role of nanocomposites in lowering the energy barrier for HER, with cobalt facilitating electron transfer from carbon to MoS_2. This approach provides a scalable method for designing 2D-2D superlattice electrocatalysts for overall water splitting in alkaline conditions. The assembled Pt/C||Co-1T-MoS_2/C cell achieves 10 mA cm^{-2} at only 1.57 V, highlighting its practical efficiency for water splitting.

Chen et al. demonstrate that Co-doped 1T-MoS_2 coupling with V_2C MXene [163] can enhance the electronic structure to optimize hydrogen adsorption and reduce overpotentials to 70.1 mV at 10 mA cm^{-1} in 1.0 M KOH. In detail, V_2C MXene was utilized as a conductive substrate in the Co–MoS_2/V_2C@CC nanohybrid, enhancing charge transfer and stabilizing the 1T-phase MoS_2 for improved HER performance. Besides, the doping effect facilitates a phase transition from 2H to 1T MoS_2, increasing the metallic character and active site density, as supported by a higher 1T phase content of approximately 70.4%. The incorporation of Co also lowers the d-band center to −1.65 eV, improving the balance between hydrogen adsorption and desorption, which accelerates HER kinetics. Additionally, the integration of V_2C MXene into the Co–MoS_2 nanocomposite further amplifies this effect by forming heterogeneous interfaces that enhance charge transfer and reduce the water dissociation energy barrier to 1.83 eV. In detail, V_2C MXene acts as a conductive scaffold, promoting electron mobility and stabilizing the 1T-MoS_2 phase, as evidenced by a high 70.4% 1T content in the Co–MoS_2/V_2C@CC hybrid. The expanded interlayer spacing of MoS_2, induced by V_2C coupling, further boosts active site availability, enhancing catalytic kinetics with the heterogeneous interface enhancing the electrochemically active surface area, with a C_{dl} value of 25.8 mF cm^{-2}, contributing to high HER performance. Additionally, the robust interfacial coupling ensures outstanding stability, with no degradation observed over 50 h at 50 mA cm^{-2}. These findings highlight the pivotal roles of Co doping and V_2C MXene in engineering the high-performance of nanocomposites.

Another type of nanocomposite involves multiple-element compositions, where various elements are combined to form hybrid structures with enhanced properties. These nanocomposites often integrate transition metal compounds with other metallic or non-metallic elements to optimize electrocatalytic performance, such as in hydrogen evolution reactions, by tailoring electronic and structural characteristics [164, 165]. In the context of the $Co_xNi_{1-x}Se_2$@$Co(OH)_2$/nickel foam (CNSC/NF) from the study of Jiang et al. [166], the integration of cobalt, nickel, and selenium forms a $Co_xNi_{1-x}Se_2$ structure, enhanced by Co $(OH)_2$ and supported on nickel foam (NF), optimizing electrocatalytic performance for hydrogen evolution through tailored electronic and structural features. In detail, a nanorod-shaped CNSC/NF catalyst was synthesized via a hydrothermal-γ radiation method, showcasing enhanced HER performance. The γ radiation induced an "island-like" amorphous/crystalline heterostructure, increasing active site density and structural stability. The Ni–Se–Co electron bridges, formed through cobalt doping, facilitate asymmetric d-p-d orbital hybridization, optimizing charge distribution at Ni sites. This mechanism enhances H_2O dissociation and H* intermediate adsorption, driving efficient HER kinetics. The catalyst achieved a low overpotential of 80 mV at 10 mA cm^{-2} in 1 M KOH, with a Tafel slope of 65 mV dec^{-1}, indicating rapid reaction rates. The robust "ball-stick" configuration and three-dimensional mass transfer interface further improve catalytic efficiency. Experimental and DFT analyses confirm that cobalt doping lowers the energy barrier for H_2O dissociation, boosting HER activity. The optimized catalyst exhibits exceptional stability, maintaining performance at 130 mA cm^{-2} for over 50 h with a retention rate of 97.4% due to its robust amorphous/crystalline heterointerfaces and further demonstrates exceptional durability in an alkaline anion exchange membrane electrolyzer for over 1000 h even at a high current density of 1 A cm^{-2}. The $Co_xNi_{1-x}Se_2$ component enhances HER activity by optimizing charge distribution and lowering H_2O dissociation barriers through Ni–Se–Co electron bridges, while the $Co(OH)_2$ nanorod array provides a stable structural template that supports in-situ growth and improves mechanical integrity. The nickel foam substrate further contributes to stability by offering a conductive, three-dimensional support that facilitates efficient electron transfer and mass transport. The scalable synthesis method highlights its potential for industrial hydrogen production.

Remarkably, Yi et al. very recently synthesized Cu single atoms on thermally stable 1T′-TMDs hollow structures (1T′-TMDs HSs) by etching $Cu_{1.94}S$ templates from pre-synthesized $Cu_{1.94}S$@TMDs, including 1T′-MoS_2, $MoSe_2$, WS_2, and WSe_2 HSs (Fig. 11) [167]. In detail, the synthesis of 1T′-TMDs HSs involves a scalable method where $Cu_{1.94}S$ templates are initially formed and used as substrates for the in situ growth of 1T′-TMD monolayers, such as MoS_2, via a one-pot colloidal chemical process. Subsequently, the $Cu_{1.94}S$ cores are removed through acid etching, yielding hollow 1T′-TMDs HSs, including $MoSe_2$, WS_2, and WSe_2, with the etched Cu ions adsorbing onto the surface as single atoms. This approach ensures high 1T′ phase purity and can be universally applied across various TMD materials (Fig. 11a). In detail, the synthesis of 1T′-MoS_2 hollow structures (HSs) begins with the preparation of $Cu_{1.94}S$ nanoplates (~83 nm diameter), followed by rapid colloidal chemical growth of MoS_2 monolayers on their surfaces within 1 min to form $Cu_{1.94}S$@MoS_2 core-shell heterostructures, as illustrated schematically and shown in the TEM image (Fig. 11b). HAADF-STEM imaging and corresponding EDX elemental mappings confirm the uniform distribution of Mo, S, and Cu elements, verifying the successful conformal coating of MoS_2 on the $Cu_{1.94}S$ nanoplate surfaces (Fig. 11e). Subsequently, the $Cu_{1.94}S$ cores are selectively etched away to yield high-yield 1T′- MoS_2 HSs, with TEM images clearly depicting the hollow morphology (Fig. 11c and d). Post-etching STEM-EDX mappings reveal the retained contour of Cu signals, likely due to adsorbed Cu ions as single atoms (SAs) or clusters on the 1T′- MoS_2 HS surfaces, which contribute to stabilizing the metastable 1T′ phase (Fig. 11f). This

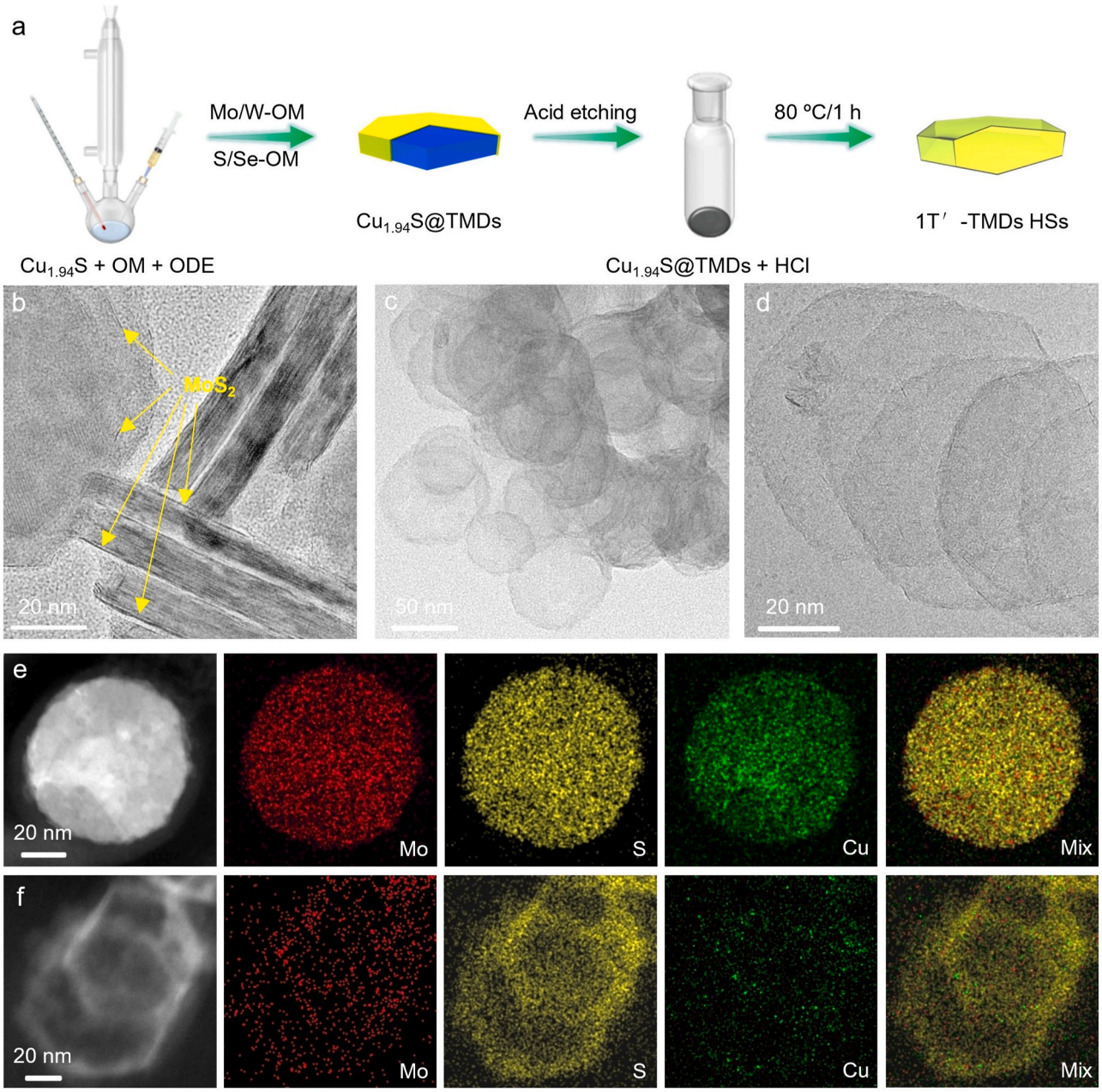

Fig. 11. (a) Synthesis procedure of 1T′-TMDs HSs. (b) TEM image of $Cu_{1.94}S@MoS_2$. (c,d) TEM images of 1T′-MoS_2 HSs by etching $Cu_{1.94}S$ from the (b) $Cu_{1.94}S@MoS_2$. HAADF-STEM image and corresponding STEM EDX elemental mappings of (e) $Cu_{1.94}S@MoS_2$ and (f) 1T′-MoS_2 HSs. Reused with permission from ref. [167] Wiley-VCH, Copyright© 2025.

template-etching strategy provides a scalable route to thermally stable 1T′-TMD hollow structures, with the process ensuring phase purity and structural integrity throughout. Advanced characterization of the 1T′-MoS_2 HSs confirmed the successful integration of Cu SAs on the surface with a Cu loading of approximately 1.7 wt%.

The optimized 1T′-MoS_2 HSs electrocatalyst exhibits an overpotential of 147 mV at 10 mA cm^{-2} and a Tafel slope of 42.4 mV dec^{-1}, indicating excellent HER kinetics compared to other 1T′-TMD HSs like $MoSe_2$, WS_2, and WSe_2, as seen in Fig. 12a and b. Its superior performance is further supported by a high turnover frequency (TOF) of 1.34 s^{-1} at 200 mV (Fig. 12c) and a large ECSA of 37.06 mF cm^{-2}, attributed to the hollow structure and synergistic effects with Cu SAs. Fig. 12d demonstrates the excellent durability of 1T′-MoS_2 HSs, with nearly overlapping LSV curves before and after 10,000 CV cycles. Fig. 12e positions 1T′-MoS_2 HSs favorably in comparisons of Tafel slope and stability against other Mo-based acidic HER catalysts, while Fig. 12f highlights its superior long-term stability, maintaining unchanged activity after 200 h of continuous operation at 1.0 A cm^{-2}, in stark contrast to the rapid decay observed for pure 1T′-MoS_2. The mechanism underlying the enhanced HER activity of Cu SAs-anchored 1T′-MoS_2 is explored through DFT calculations (Fig. 12g–i), which show that Cu SAs modify the ΔG_{H^*} to values closer to zero. Specifically, Fig. 12h exhibited that ΔG_{H^*} values are calculated to be 0.317 eV at the Cu-coordinated S1 site (Cu-1T′-MoS_2-S1), - 0.050 eV at the adjacent S2 site (Cu-1T′-MoS_2-S2), and 0.096 eV when H adsorbs directly on Cu (Cu-1T′-MoS_2-Cu), all markedly improved over the 0.399 eV of 1T′-MoS_2-S. The best performance occurs at the S2 site neighboring the Cu atom rather than the directly coordinated site, demonstrating that Cu SAs indirectly enhance HER activity by modulating the electronic structure of nearby sulfur atoms through strong metal-support interactions. Further engineering

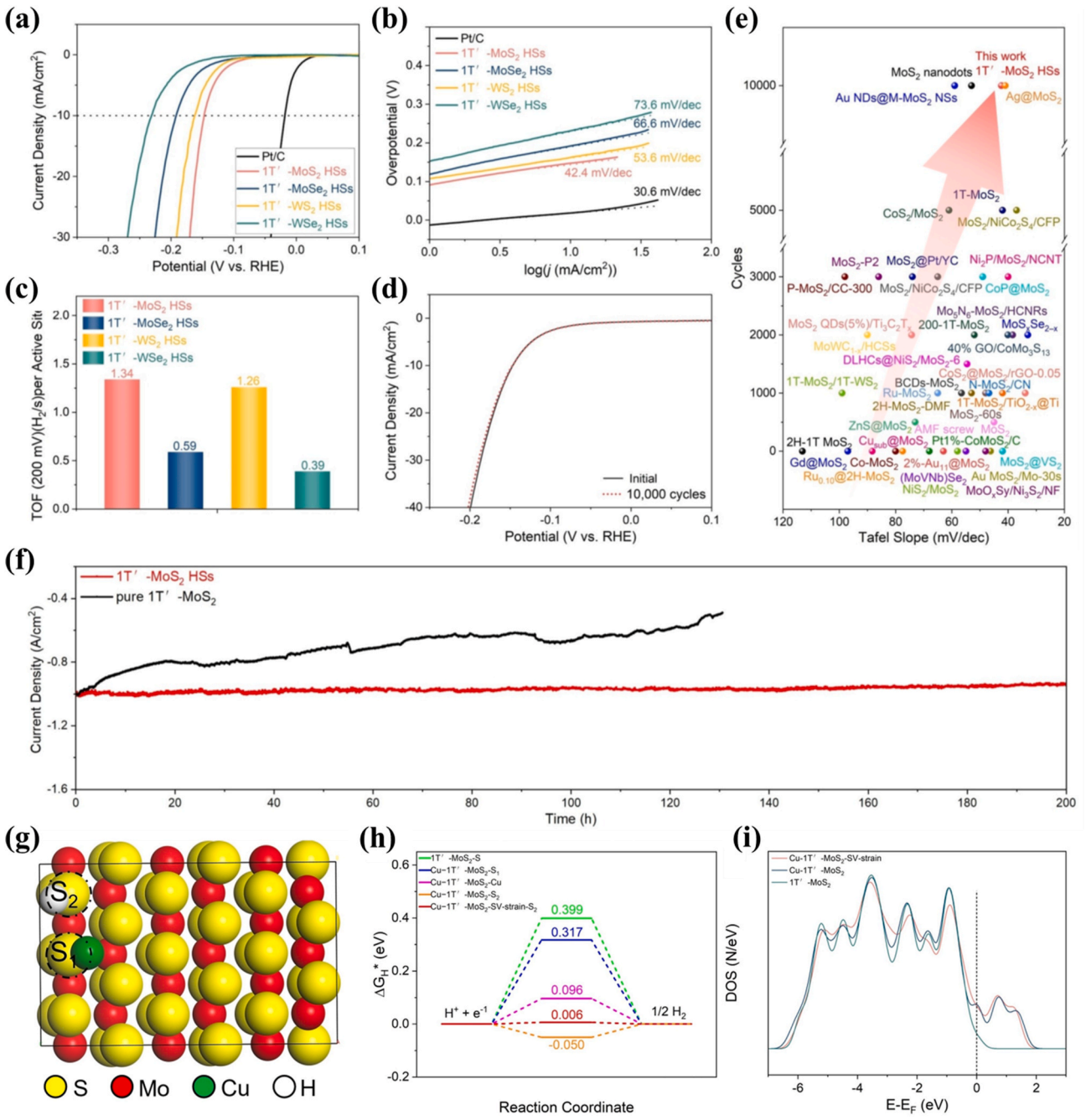

Fig. 12. (a) LSV curves. (b) Tafel slope. (c) TOF values. (d) LSV curves of 1T′-MoS_2 HSs before and after 10,000 CV cycles. (e) Comparison of Tafel slope and catalytic stability of 1T′-MoS_2 HSs and Mo-based electrocatalysts in acidic electrolyte. (f) Comparison of catalytic stability of 1T′-MoS_2 HSs and pure 1T′-MoS_2 by i-t curve test at 1.0 A cm^{-2}. Structural models of (g) Cu-1T′-MoS_2-SV-strain (black circles S_1 and S_2 represent different active sites). (h) The ΔG_{H^*} of the various active sites in 1T′-MoS_2 and Cu-1T′-MoS_2. (i) DOS analysis of Cu-1T′-MoS_2-SV-strain, Cu-1T′-MoS_2, and 1T′-MoS_2. Reused with permission from ref. [167] Wiley-VCH, Copyright© 2025.

the S2 site by introducing 1.5% tensile strain and sulfur vacancies yields an exceptionally low ΔG_{H^*} of only 0.006 eV (Cu-1T′-MoS_2-SV-strain-S2), highlighting the synergistic positive effect of lattice strain and vacancies on catalytic performance. Density of states analysis (Fig. 12i) shows that the combined incorporation of Cu SAs, vacancies, and strain results in more pronounced DOS peaks near the Fermi level, indicating significantly improved electrical conductivity of the system. The introduction of lattice strain and sulfur vacancies further boosts conductivity and catalytic efficiency, aligning with experimental observations of improved performance.

The HER is significantly enhanced by the $Co(OH)_2$/Mo-VS_2 nanocomposite, as reported by Wang et al. [168], achieving a low overpotential of 41 mV at 10 mA cm^{-2} in 1.0 M KOH. The Mo-VS_2 component plays a critical role by doping vanadium disulfide, optimizing its electronic structure through charge redistribution, which facilitates water dissociation and improves H* adsorption energy. Meanwhile, the $Co(OH)_2$ component contributes by enhancing water adsorption and activation, acting as primary sites for the Volmer step in the HER mechanism. The synergistic interaction between these components is further amplified by interfacial electron transfer, reducing the Tafel slope to 117 mV dec^{-1}, indicative of a Volmer-Heyrovsky mechanism with efficient H_2 release. DFT calculations reveal that S sites in Mo-VS_2, with a ΔG_{H^*} of 0.101 eV, excel at H* binding, while Co sites in $Co(OH)_2$ promote initial water activation, creating a spatial synergy that

accelerates the reaction. The nanocomposite's increased electrochemical active surface area, evidenced by a C_{dl} of 9.28 mF cm^{-2}, ensures more exposed active sites, boosting overall HER performance. This dual-modulation strategy leverages the distinct roles of each component, enhancing charge transfer kinetics as confirmed by EIS analysis.

The HER performance of the NiCo–MoS_2-carbonized wood nanocomposite, as reported by Hu et al. [169], is also markedly improved, achieving an overpotential of 64 mV at 10 mA cm^{-2} in 1.0 M KOH, showcasing its efficiency. The MoS_2 component, structured as nanoflowers with 1T/2H phases, enhances active site exposure and catalytic activity, while NiCo modification optimizes the electronic structure, promoting the Volmer step in the HER mechanism with a Tafel slope of 89.5 mV dec^{-1}, indicative of a Volmer-Heyrovsky process. The carbonized wood substrate boosts conductivity and stability, supporting the durability over 24 h at 64 mV with minimal current decay. XPS analysis confirms NiCo induces weak electron characteristics, facilitating H_2O ionization and H^+ adsorption, critical for sustained HER kinetics. This synergy results in a high electrochemical double-layer capacitance of 201.6 mF cm^{-2}, reflecting an increased active surface area.

In summary, nanocomposite approaches mainly improve HER by combining TMS/TMSe active components with highly conductive, large-surface-area matrices like carbon-based materials, MXene, nickel foam, or hollow frameworks. The key advantages stem from enhanced electrical conduction throughout the electrode, even distribution of active particles, reduced particle clumping or degradation, expanded electrochemically accessible area, and greater mechanical and chemical resilience, though they sometimes prioritize extrinsic enhancements over maximal intrinsic activity. Multi-component variants additionally refine charge distribution and reaction dynamics through tailored elemental interactions. Such hybrids deliver competitive overpotentials and Tafel slopes coupled with impressive endurance. In comparison to heterostructures, the enhancement here is largely matrix-supported, emphasizing practical improvements in transport and longevity rather than direct interfacial catalysis. The fundamental principle is that robust conductive hosts facilitate viable, large-scale electrode fabrication, making nanocomposites indispensable for translating laboratory results into industrially relevant hydrogen production technologies.

4. Perspectives on challenges and prospects

Despite notable advancements in the development of TMS/TMSe electrocatalysts for HER (Table 1), key barriers persist in achieving industrial viability. For example, the basal planes in materials such as MoS_2 and WS_2 limit the catalytic activity primarily to the edge sites. While strategies such as defect engineering can activate the basal planes, implementing this with precision and scalability at low cost remains difficult. The poor electrical conductivity of the 2H phase also poses a limitation, increasing the overpotential required for HER. While the transition to the metallic 1T phase and the formation of conductive composites can mitigate this, stabilizing the 1T phase on a large scale is complex, as the 1T and 2H phases often coexist in synthesized materials. Long-term durability in aggressive electrolytes or at industrial currents (>1 A cm^{-2}) is another weak point, with many catalysts prone to aggregation, Cl^--induced corrosion in seawater, or dissolution, as evidenced by stability drops after mere hours in some heterostructures.

Table 1
The catalytic activity comparison of representative TMS- and TMSe-based electrocatalysts for HER with corresponding strategies.

Strategy	Catalyst	Electrolyte	η (mV)	j (mA cm^{-2})	b (mV dec^{-1})	Ref.
Morphology	$MoSe_2$-CTAB@F68	0.5 M H_2SO_4	189	10	62	[103]
	WS_2/WO_3 nanorod	0.5 M H_2SO_4	224	10	82.7	[106]
	MoS_2/WS_2 nanoflower	0.5 M H_2SO_4	251	10	61	[107]
	WS_2/W_2C nano hollow flowers	0.5 M H_2SO_4	280	10	61	[92]
	$MoSe_2/CoSe_2$ nano-flakes	1 M KOH	137	10	55.9	[99]
	$NiSe_2$/CoSe/NF-3.0 microflower	1 M KOH	148	10	88.6	[110]
Phase	1T′-MoS_2	0.5 M H_2SO_4	149	10	42	[104]
	$MoSe_{2.3}$	0.5 M H_2SO_4	130	10	46	[112]
	Mo@(2H,1T)-$MoSe_2$	0.5 M H_2SO_4	183	20	72	[115]
	$Ni(OH)_2$/1T-MoS_2/CC	1 M KOH	216	250	70.8	[170]
Defect and Phase	Defect-rich 1T-MoS_2	0.5 M H_2SO_4	153	10	43	[125]
Defect	S vacancy-rich MoS_2	0.5 M H_2SO_4	148	10	51.6	[127]
	NiS_2-Vs 5.9%	1 M KOH	108	10	82	[128]
	$Ni_3S_2/MoS_2(V_{g10})$	1 M KOH	84	10	61.6	[129]
Doping	Fe doped MoS_2	0.5 M H_2SO_4	173	10	40.1	[134]
	mPF-Co-MoS_2	0.5 M H_2SO_4	156	10	74	[135]
	$Ni_{0.05}Mo_{0.95}S_2$	0.5 M H_2SO_4	215	10	62	[136]
	1T-MoS_2-Pt (14.3 wt% Pt)	1.0 M KOH + 0.5 M NaCl (simulated seawater)	123	10	64	[138]
	P-doped $MoSe_2$/CFP	0.5 M H_2SO_4	186	50	54.3	[139]
	(Mo, N)–$NiSe_2$	1 M KOH	82	10	84.5	[140]
	$Co_{0.18}$/1T-$Mo_{0.82}S_2$@N-rGO	1 M KOH	142	10	48	[137]
Heterostructures	1T-WS_2/1T-WSe_2	0.5 M H_2SO_4	291	10	57	[153]
	$NiSe_2/MoSe_2$	0.5 M H_2SO_4	147	10	43.5	[171]
	0.2$CoSe_2/MoSe_2$	1 M KOH	218	10	76	[148]
	$NiCo_2S_4/Co_9S_8$	1 M KOH	172	10	115	[149]
	$NiSe_2$/NiS	1 M KOH	155	10	101	[152]
	Mo_3Se_4–NiSe	1 M KOH	84.4	10	59.6	[147]
	MoS_2@o-$CoSe_2$	1 M KOH	34	10	41	[154]
	Co_9S_8/MnS/MoS_2/NF	1 M KOH	85	10	76.9	[145]
	Nd_2Se_3–Mn_2O_3	1 M KOH	121	10	78	[172]
	$MoSe_2$–Ni_3S_2	1 M KOH	171	10	45	[173]
	$NiSe_2$–$RuSe_2$	1 M KOH + sea water	26	10	46.2	[151]
Nanocomposites	GDY/CoS_2/CC	1 M KOH	97	10	56	[146]
	Co-doped 1T-MoS_2-V_2C MXene	1 M KOH	70.1	10	98.6	[163]
	V-$NiMoSe_x$	1 M KOH	37.8	10	40.2	[174]
	Co-1T-MoS_2/C	1 M KOH	135	10	88.3	[162]
	$Co_xNi_{1-x}Se_2$@$Co(OH)_2$/NF	1 M KOH	80	10	65	[166]
	$Co(OH)_2$/Mo-VS_2	1 M KOH	41	10	117	[168]
	NiCo–MoS_2-Carbonized wood	1 M KOH	64	10	89.5	[169]

Additionally, the scalability of synthesis methods is another critical aspect. While CVD can produce high-quality catalysts, it is often costly, energy-intensive, and less scalable compared to hydrothermal methods, which can sometimes produce variable results. Furthermore, a complete understanding of the catalytic reaction mechanisms, especially in neutral media, is still lacking. The detailed HER mechanism in bimetallic sulfides, complex heterostructures, and highly defective materials is still in its preliminary stages of understanding. Thus, a deeper, atomistic-level comprehension is necessary for truly rational design. Finally, despite the advancements, a performance gap still exists between metal disulfide catalysts and platinum, particularly in terms of overpotential and exchange current density.

To advance, research must prioritize innovative defect and phase control, such as plasma-assisted vacancy tuning for site-specific activation or alloyed dopants to lock in 1T phases without high temperatures. Exploring unconventional dopants like rare-earth elements or high-entropy configurations could unlock untapped electronic synergies, while advanced heterostructures incorporating quantum-confined layers promise tailored interfaces for pH-universal activity. Hierarchical morphologies via template-free methods remain vital for exposing edges affordably.

Integrating fields like computational materials science and AI will be transformative for TMS/TMSe optimization. Machine learning could predict defect patterns from vast datasets, guiding synthesis for minimal overpotentials, while in-situ techniques like operando TEM reveal real-time phase shifts. High-throughput AI screening might identify novel compositions, forecasting metrics like Tafel slopes with 90% accuracy to expedite experiments. Deeper mechanistic probes via ab initio simulations and experiments are essential, especially for seawater HER, where pH gradients and ion poisoning alter kinetics. Current DFT often ignores solvation, voltage, and pH effects, leading to discrepancies; future models should incorporate grand-canonical ensembles and explicit electrolytes for more realistic predictions.

Addressing stability and scalability challenges is essential to translate TMS/TMSe catalysts from lab to industry. Among these strategies discussed above, nanocomposites and morphology engineering show the most promise for scalability due to their reliance on straightforward, one-step methods like hydrothermal synthesis or support hybridization, enabling cost-effective, large-scale production for industrial hydrogen evolution that enables kg-scale production at $<$10% of CVD costs. Furthermore, innovative approaches, such as bio-mimetic designs inspired by hydrogenase enzymes, could embed active motifs in protective matrices for multi-electrolyte resilience. Eco-conscious syntheses, like ambient-pressure solvothermal processes using biomass-derived solvents, will cut environmental footprints while scaling output.

Looking ahead, commercializing TMS/TMSe electrocatalysts demands prioritizing processability and seamless integration into real-world systems, such as anion-exchange-membrane (AEM) or proton-exchange-membrane (PEM) electrolyzers optimized for intermittent renewable inputs. Monolithic or thin film architectures, for instance, could substantially improve mechanical robustness against delamination and enable roll-to-roll fabrication at scales rivaling solar panel production, far surpassing the handling limitations of conventional powder catalysts. By harnessing high-throughput computational screening to predict defect-tolerant compositions, adopting green synthesis routes like microwave-assisted hydrothermal processes to reduce energy use by 50-70%, and drawing cross-disciplinary insights from electrochemistry and nanoscience, the field can surmount barriers like inconsistent batch quality and establish TMS/TMSe as pivotal enablers of carbon-neutral hydrogen economies. Academia-industry collaborations, through targeted consortia for pilot-scale testing, will be vital to iteratively refine these strategies, critically evaluating trade-offs like activity losses from protective coatings while validating performance under variable conditions such as fluctuating pH or impurity-laden feeds. Ultimately, these focused advancements will expedite TMS/TMSe adoption in renewable energy infrastructures, critically advancing global sustainability by delivering hydrogen production costs below $2/kg through enhanced efficiency and durability.

5. Conclusion

TMS and TMSe present a cost-effective and abundant alternative to platinum for the hydrogen evolution reaction. Motivated by the pressing demand for sustainable and economical hydrogen production, these earth-abundant materials are increasingly recognized as viable substitutes for costly noble metal catalysts. Despite the promising attributes of metal disulfides, challenges such as the inertness of basal planes, limited conductivity, and stability issues persist. However, significant progress has been made in recent years through various structural engineering strategies, including morphology and phase engineering (stabilizing the 1T metallic phase), defect and doping with various elements, the formation of heterostructures, and making nanocomposites with other conductive materials. These advancements have led to substantial improvements in the catalytic performance of metal disulfides, with some recent catalysts even showing the potential to surpass platinum in specific metrics. While the journey towards replacing noble metals entirely for industrial-scale hydrogen production requires continued research and innovation, the remarkable progress in the field of TMS and TMSe electrocatalysts offers a promising pathway towards a sustainable hydrogen economy.

CRediT authorship contribution statement

Dang Le Tri Nguyen: Writing – review & editing, Writing – original draft, Methodology, Formal analysis, Data curation, Conceptualization. **Vinh Van Tran:** Methodology, Investigation, Formal analysis, Data curation. **Chinh Chien Nguyen:** Methodology, Investigation, Formal analysis, Data curation. **Tung M. Nguyen:** Writing – review & editing, Supervision, Resources, Project administration, Conceptualization.

Declaration of competing interest

The authors declare that they have no known competing financial interests or personal relationships that could have appeared to influence the work reported in this paper.

Acknowledgements

The authors acknowledge the financial support received from Chalmers University of Technology, Sweden. Authors Dang L. T. Nguyen and Tung M. Nguyen specifically wish to thank Dr. An Vu Thuy Tran and Ms. Ngoc Bich Nguyen, respectively, for their endless and valuable support.

Data availability

Data will be made available on request.

References

[1] Seh ZW, Kibsgaard J, Dickens CF, Chorkendorff I, Nørskov JK, Jaramillo TF. Combining theory and experiment in electrocatalysis: insights into materials design. Science 2017;355:4998.
[2] Nikolaidis P, Poullikkas A. A comparative overview of hydrogen production processes. Renew Sustain Energy Rev 2017;67:597–611.
[3] Zhang X, Jia F, Song S. Recent advances in structural engineering of molybdenum disulfide for electrocatalytic hydrogen evolution reaction. Chem Eng J 2021;405:127013.
[4] Roger I, Shipman MA, Symes MD. Earth-abundant catalysts for electrochemical and photoelectrochemical water splitting. Nat Rev Chem 2017;1:3.
[5] Chen Z, Duan X, Wei W, Wang S, Ni B-J. Recent advances in transition metal-based electrocatalysts for alkaline hydrogen evolution. J Mater Chem A 2019;7:14971–5005.
[6] Züttel A, Remhof A, Borgschulte A, Friedrichs O. Hydrogen: the future energy carrier. Philos Trans A Math Phys Eng Sci 2010;368:3329–42.

[7] Najaf Z, Nguyen DLT, Chae SY, Joo O-S, Shah AUHA, Vo D-VN, et al. Recent trends in development of hematite (α-Fe2O3) as an efficient photoanode for enhancement of photoelectrochemical hydrogen production by solar water splitting. Int J Hydrogen Energy 2021;46:23334–57.

[8] Mahmood N, Yao Y, Zhang J-W, Pan L, Zhang X, Zou J-J. Electrocatalysts for hydrogen evolution in alkaline electrolytes: mechanisms, challenges, and prospective solutions. Adv Sci 2018;5:1700464.

[9] Megía PJ, Vizcaíno AJ, Calles JA, Carrero A. Hydrogen production technologies: from fossil fuels toward renewable sources. A mini review. Energy Fuels 2021;35:16403–15.

[10] Tüysüz H. Alkaline water electrolysis for green hydrogen production. Acc Chem Res 2024;57:558–67.

[11] Munir A, Abdul Nasir J, Haq Tu, Iqbal J, Hussain I, Qurashi A. Benchmarking stable electrocatalysts for green hydrogen production: a chemist perspective. Coord Chem Rev 2024;521:216112.

[12] Nguyen V-H, Nguyen TP, Le T-H, Vo D-VN, Nguyen DLT, Trinh QT, et al. Recent advances in two-dimensional transition metal dichalcogenides as photoelectrocatalyst for hydrogen evolution reaction. J Chem Tech Biotechnol 2020. n/a.

[13] Zhang J, Zhang Q, Feng X. Support and interface effects in water-splitting electrocatalysts. Adv Mater 2019;31:1808167.

[14] Zhu J, Hu L, Zhao P, Lee LYS, Wong K-Y. Recent advances in electrocatalytic hydrogen evolution using nanoparticles. Chem Rev 2020;120:851–918.

[15] Wang T, Li J, Xiao L, Gao S, Yu J, Liu W, et al. Recent advances in transition metal sulphide-based electrocatalysts for the oxygen and hydrogen evolution reactions. Surf Interfaces 2025;70:106784.

[16] Feidenhans'l AA, Regmi YN, Wei C, Xia D, Kibsgaard J, King LA. Precious metal free hydrogen evolution catalyst design and application. Chem Rev 2024;124:5617–67.

[17] Tran DT, Tran PKL, Malhotra D, Nguyen TH, Nguyen TTA, Duong NTA, et al. Current status of developed electrocatalysts for water splitting technologies: from experimental to industrial perspective. Nano Converg 2025;12:9.

[18] Do HH, Nguyen THC, Nguyen TV, Xia C, Nguyen DLT, Raizada P, et al. Metal-organic-framework based catalyst for hydrogen production: progress and perspectives. Int J Hydrogen Energy 2022.

[19] Kong D, Cha JJ, Wang H, Lee HR, Cui Y. First-row transition metal dichalcogenide catalysts for hydrogen evolution reaction. Energy Environ Sci 2013;6:3553–8.

[20] Liu G, Ding L, Meng Y, Ali A, Zuo G, Meng X, et al. A review on ultra-small undoped MoS_2 as advanced catalysts for renewable fuel production. Carbon Energy 2024;6:e521.

[21] Fang M, Dong G, Wei R, Ho JC. Hierarchical nanostructures: design for sustainable water splitting. Adv Energy Mater 2017;7:1700559.

[22] Nguyen TV, Le QV, Nguyen CC, Nguyen TP, Dao DV, Cho JH, et al. Synthesis of nano-coral tungsten carbide/carbon fibers as efficient catalysts for hydrogen evolution reaction. Int J Energy Res 2022;46:13089–98.

[23] Abghoui Y, Skúlason E. Hydrogen evolution reaction catalyzed by transition-metal nitrides. J Phys Chem C 2017;121:24036–45.

[24] Liu Y, Yu G, Li G-D, Sun Y, Asefa T, Chen W, et al. Coupling Mo_2C with nitrogen-rich nanocarbon leads to efficient hydrogen-evolution electrocatalytic sites. Angew Chem Int Ed 2015;54:10752–7.

[25] Wu R, Zhang H, Ma H, Zhao B, Li W, Chen Y, et al. Synthesis, modulation, and application of two-dimensional TMD heterostructures. Chem Rev 2024;124:10112–91.

[26] Van Nguyen T, Tekalgne M, Nguyen TP, Van Le Q, Ahn SH, Kim SY. Electrocatalysts based on MoS_2 and WS_2 for hydrogen evolution reaction: an overview. Battery Energy 2023;2:20220057.

[27] Wang T, Xie H, Chen M, D'Aloia A, Cho J, Wu G, et al. Precious metal-free approach to hydrogen electrocatalysis for energy conversion: from mechanism understanding to catalyst design. Nano Energy 2017;42:69–89.

[28] Agyapong-Fordjour FO-T, Yun SJ, Kim H-J, Choi W, Kirubasankar B, Choi SH, et al. Substitutional vanadium sulfide nanodispersed in MoS_2 film for Pt-Scalable catalyst. Adv Sci 2021;8:2003709.

[29] Zhang Y, Zhou Q, Zhu J, Yan Q, Dou SX, Sun W. Nanostructured metal chalcogenides for energy storage and electrocatalysis. Adv Funct Mater 2017;27:1702317.

[30] Shuai H, Liu R, Li W, Yang X, Lu H, Gao Y, et al. Recent advances of transition metal sulfides/selenides cathodes for aqueous zinc-ion batteries. Adv Energy Mater 2023;13:2202992.

[31] Roy S, Joseph A, Zhang X, Bhattacharyya S, Puthirath AB, Biswas A, et al. Engineered two-dimensional transition metal dichalcogenides for energy conversion and storage. Chem Rev 2024;124:9376–456.

[32] Xie S, Sun B, Sun H, Zhan K, Zhao B, Yan Y, et al. Engineering of molybdenum sulfide nanostructures towards efficient electrocatalytic hydrogen evolution. Int J Hydrogen Energy 2019;44:15009–16.

[33] Xu X, Song F, Hu X. A nickel iron diselenide-derived efficient oxygen-evolution catalyst. Nat Commun 2016;7:12324.

[34] Nguyen TM, Tran MX, Nguyen TV, Dang HT, Le QV, Kim SY, et al. Embedding nickel diselenide in carbon derived from biomass and its electrocatalytic activity for hydrogen evolution reaction. Int J Hydrogen Energy 2024;52:709–17.

[35] Wang F, Li Y, Shifa TA, Liu K, Wang F, Wang Z, et al. Selenium-enriched nickel selenide nanosheets as a robust electrocatalyst for hydrogen generation. Angew Chem Int Ed 2016;55:6919–24.

[36] Li R, Xie S, Zeng Y, Zhao Q, Mao M, Liu Z, et al. Synergistic dual-regulating the electronic structure of NiMo selenides composite for highly efficient hydrogen evolution reaction. Fuel 2024;358:130203.

[37] Ji J, Choi JH. Recent progress in 2D hybrid heterostructures from transition metal dichalcogenides and organic layers: properties and applications in energy and optoelectronics fields. Nanoscale 2022;14:10648–89.

[38] Browne MP, Sofer Z, Pumera M. Layered and two dimensional metal oxides for electrochemical energy conversion. Energy Environ Sci 2019;12:41–58.

[39] Yan M, Pan X, Wang P, Chen F, He L, Jiang G, et al. Field-effect tuned adsorption dynamics of VSe_2 nanosheets for enhanced hydrogen evolution reaction. Nano Lett 2017;17:4109–15.

[40] Kagkoura A, Canto-Aguilar EJ, Gracia-Espino E, Zeng L, Olsson E, Oliveira FM, et al. Cobalt- and nickel-doped WSe_2 as efficient electrocatalysts for water splitting and as cathodes in hydrogen evolution reaction proton exchange membrane water electrolysis. J Phys Chem C 2025;129:2893–903.

[41] Li R, Li Y, Yang P, Wang D, Xu H, Wang B, et al. Electrodeposition: synthesis of advanced transition metal-based catalyst for hydrogen production via electrolysis of water. J Energy Chem 2021;57:547–66.

[42] Jia H, Meng L, Lu Y, Liang T, Yuan Y, Hu Y, et al. Boosting the efficiency of electrocatalytic water splitting via in situ grown transition metal sulfides: a review. J Mater Chem A 2024;12:28595–617.

[43] Li W, Wang C, Lu X. Integrated transition metal and compounds with carbon nanomaterials for electrochemical water splitting. J Mater Chem A 2021;9:3786–827.

[44] Karunadasa HI, Montalvo E, Sun Y, Majda M, Long JR, Chang CJ. A molecular MoS_2 edge site mimic for catalytic hydrogen generation. Science 2012;335:698–702.

[45] Tsai C, Abild-Pedersen F, Nørskov JK. Tuning the MoS_2 edge-site activity for hydrogen evolution via support interactions. Nano Lett 2014;14:1381–7.

[46] Wu H, Huang Q, Shi Y, Chang J, Lu S. Electrocatalytic water splitting: mechanism and electrocatalyst design. Nano Res 2023;16:9142–57.

[47] Kazemi A, Manteghi F, Tehrani Z. Metal electrocatalysts for hydrogen production in water splitting. ACS Omega 2024;9:7310–35.

[48] Toan TTT, Nguyen DM, Dao AQ, Le VT, Vasseghian Y. Latest insights on metal-based catalysts in the electrocatalysis processes: challenges and future perspectives. Mol Catal 2023;538:113001.

[49] Do HH, Le QV, Nguyen TV, Huynh KA, Tekalgne MA, Tran VA, et al. Synthesis of MoS_x/Ni-metal-organic framework-74 composites as efficient electrocatalysts for hydrogen evolution reactions. Int J Energy Res 2021;45:9638–47.

[50] Wu C, Liu J, Tan Y. Transition metal sulfides in alkaline hydrogen evolution electrocatalysis: Re-exploring their structure and composition evolution and its correlation with activity. Nano Res 2025;18:94907240.

[51] Ding Y, Gao Z, Xiang H. Synthesis and structural engineering of transition metal sulfides: advances in improving hydrogen evolution reaction catalytic efficiency. INORGA 2025.

[52] Majhi KC, Yadav M. Transition metal-based chalcogenides as electrocatalysts for overall water splitting. ACS Eng Au 2023;3:278–84.

[53] Chang K, Hai X, Pang H, Zhang H, Shi L, Liu G, et al. Targeted synthesis of 2H- and 1T-Phase MoS_2 monolayers for catalytic hydrogen evolution. Adv Mater 2016;28:10033–41.

[54] Chen S, Liu X, Xiong J, Mi L, Song X-Z, Li Y. Defect and interface engineering in metal sulfide catalysts for the electrocatalytic nitrogen reduction reaction: a review. J Mater Chem A 2022;10:6927–49.

[55] Tan ZH, Kong XY, Ng B-J, Soo HS, Mohamed AR, Chai S-P. Recent advances in defect-engineered transition metal dichalcogenides for enhanced electrocatalytic hydrogen evolution: perfecting imperfections. ACS Omega 2023;8:1851–63.

[56] Liu P, Cao J, Yuan Y, Zhang C. Recent progress of molybdenum disulfide/carbon composites for electrochemical hydrogen evolution reaction. Carbon Trends 2024;15:100364.

[57] Tuan Van N, Mahider T, Quyet Van L, Chau Van T, Sang Hyun A, Soo Young K. Recent progress and strategies of non-noble metal electrocatalysts based on MoS_2/MOF for the hydrogen evolution reaction in water electrolysis: an overview. Microstructures 2024;4:2024046.

[58] Sahu N, Das JK, Behera JN. $NiSe_2$ nanoparticles encapsulated in N-Doped carbon matrix derived from a one-dimensional Ni-MOF: an efficient and sustained electrocatalyst for hydrogen evolution reaction. Inorg Chem 2022;61:2835–45.

[59] Yu J, Li W-J, Kao G, Xu C-Y, Chen R, Liu Q, et al. In-situ growth of CNTs encapsulating P-doped $NiSe_2$ nanoparticles on carbon framework as efficient bifunctional electrocatalyst for overall water splitting. J Energy Chem 2021;60:111–20.

[60] Nguyen DLT, Nguyen N-A, Pham DD, Van Pham D, Chau NT, Nguyen NT, et al. Cassava starch residue derived activated carbon-supported low-loading ultrafine MoS_2: a sustainable and efficient catalyst for electrochemical hydrogen evolution. Int J Hydrogen Energy 2025;162:150733.

[61] Wang Z, Liu S, Duan W, Xing Y, Hu Y, Ma Y. Transition metal selenides as catalysts for electrochemical water splitting. Int J Hydrogen Energy 2024;60:1414–32.

[62] Liang T, Wang A, Ma D, Mao Z, Wang J, Xie J. Low-dimensional transition metal sulfide-based electrocatalysts for water electrolysis: overview and perspectives. Nanoscale 2022;14:17841–61.

[63] Mahajan P, Khanna V. 2D nanomaterials for photocatalytic and electrocatalytic water splitting: transforming hydrogen production for sustainable energy. Int J Hydrogen Energy 2025;145:942–69.

[64] Kumaravel S, Kundu S. Chapter 17 - sulfide and selenide-based electrocatalysts for hydrogen evolution reaction (HER). In: Dalapati G, Shun Wong T, Kundu S, Chakraborty A, Zhuk S, editors. Sulfide and selenide based materials for emerging applications. Elsevier; 2022. p. 427–63.

[65] Zhao J, Wang J, Chen Z, Ju J, Han X, Deng Y. Metal chalcogenides: an emerging material for electrocatalysis. APL Mater 2021;9:050902.

[66] Cook TR, Dogutan DK, Reece SY, Surendranath Y, Teets TS, Nocera DG. Solar energy supply and storage for the legacy and nonlegacy worlds. Chem Rev 2010; 110:6474–502.

[67] Trasatti S. Work function, electronegativity, and electrochemical behaviour of metals: III. Electrolytic hydrogen evolution in acid solutions. J Electroanal Chem Interfacial Electrochem 1972;39:163–84.

[68] Sheng W, Myint M, Chen JG, Yan Y. Correlating the hydrogen evolution reaction activity in alkaline electrolytes with the hydrogen binding energy on monometallic surfaces. Energy Environ Sci 2013;6:1509–12.

[69] Khan NA, Rahman G, Nguyen TM, Shah AUHA, Pham CQ, Tran MX, et al. Recent development of nanostructured nickel metal-based electrocatalysts for hydrogen evolution reaction: a review. Top Catal 2023;66:149–81.

[70] Medford AJ, Vojvodic A, Hummelshøj JS, Voss J, Abild-Pedersen F, Studt F, et al. From the Sabatier principle to a predictive theory of transition-metal heterogeneous catalysis. J Catal 2015;328:36–42.

[71] Nguyen DLT, Nguyen N-A, Ho TH, Nguyen TP, Dang HT, Pham DD, et al. Pumpkin shell-derived activated carbon-supported S-incorporated transition metal oxide electrocatalyst for hydrogen evolution reaction. Fuel 2024;373: 132357.

[72] Hinnemann B, Moses PG, Bonde J, Jørgensen KP, Nielsen JH, Horch S, et al. Biomimetic hydrogen evolution: MoS_2 nanoparticles as catalyst for hydrogen evolution. J Am Chem Soc 2005;127:5308–9.

[73] Wang X, Zhang Y, Si H, Zhang Q, Wu J, Gao L, et al. Single-atom vacancy defect to trigger high-efficiency hydrogen evolution of MoS_2. J Am Chem Soc 2020;142: 4298–308.

[74] Zhou W, Dong L, Tan L, Tang Q. First-principles study of sulfur vacancy concentration effect on the electronic structures and hydrogen evolution reaction of MoS_2. Nanotechnology 2021;32:145718.

[75] Li Z, Yan X, He D, Hu W, Younan S, Ke Z, et al. Manipulating coordination structures of mixed-valence copper single atoms on 1T-MoS_2 for efficient hydrogen evolution. ACS Catal 2022;12:7687–95.

[76] Wang H, Xiao X, Liu S, Chiang C-L, Kuai X, Peng C-K, et al. Structural and electronic optimization of MoS_2 edges for hydrogen evolution. J Am Chem Soc 2019;141:18578–84.

[77] Nguyen V-T, Yang T-Y, Le PA, Yen P-J, Chueh Y-L, Wei K-H. New simultaneous exfoliation and doping process for generating MX_2 nanosheets for electrocatalytic hydrogen evolution reaction. ACS Appl Mater Interfaces 2019;11:14786–95.

[78] Coogan Á, Gun'ko YK. Solution-based "bottom-up" synthesis of group VI transition metal dichalcogenides and their applications. Mater Adv 2021;2: 146–64.

[79] Kuc A, Zibouche N, Heine T. Influence of quantum confinement on the electronic structure of the transition metal sulfide ?S2. Phys Rev B 2011;83:245213.

[80] Xin H, Vojvodic A, Voss J, Nørskov JK, Abild-Pedersen F. Effects of d-band shape on the surface reactivity of transition-metal alloys. Phys Rev B 2014;89:115114.

[81] Hammer B, Nørskov JK. Electronic factors determining the reactivity of metal surfaces. Surf Sci 1995;343:211–20.

[82] Hammer B, Nørskov JK. Theoretical surface science and catalysis—calculations and concepts. Advances in catalysis. Academic Press; 2000. p. 71–129.

[83] Xiong L, Qiu Y, Peng X, Liu Z, Chu PK. Electronic structural engineering of transition metal-based electrocatalysts for the hydrogen evolution reaction. Nano Energy 2022;104:107882.

[84] Wang J, Liao T, Wei Z, Sun J, Guo J, Sun Z. Heteroatom-doping of non-noble metal-based catalysts for electrocatalytic hydrogen evolution: an electronic structure tuning strategy. Small Methods 2021;5:2000988.

[85] Kadantsev ES, Hawrylak P. Electronic structure of a single MoS_2 monolayer. Solid State Commun 2012;152:909–13.

[86] Hartmann G, Lee M, Hwang GS. Structural, electronic and adsorption properties of monolayer 2H-MoS_2 on graphene substrates: a computational study. Inorg Chem Commun 2019;106:135–8.

[87] Jaramillo TF, Jørgensen KP, Bonde J, Nielsen JH, Horch S, Chorkendorff I. Identification of active edge sites for electrochemical H_2 evolution from MoS_2 nanocatalysts. Science 2007;317:100–2.

[88] Mohammed-Ibrahim J, Sun X. Recent progress on earth abundant electrocatalysts for hydrogen evolution reaction (HER) in alkaline medium to achieve efficient water splitting – a review. J Energy Chem 2019;34:111–60.

[89] Nørskov JK, Bligaard T, Logadottir A, Kitchin JR, Chen JG, Pandelov S, et al. Trends in the exchange current for hydrogen evolution. J Electrochem Soc 2005; 152:J23.

[90] Jing F, Lv Q, Wang Q, Chi K, Xu Z, Wang X, et al. Self-supported 3D porous N-Doped nickel selenide electrode for hydrogen evolution reaction over a wide range of pH. Electrochim Acta 2019;304:202–9.

[91] Deng S, Zhong Y, Zeng Y, Wang Y, Wang X, Lu X, et al. Hollow TiO_2@Co_9S_8 core–branch arrays as bifunctional electrocatalysts for efficient oxygen/hydrogen production. Adv Sci 2018;5:1700772.

[92] Nguyen TV, Nguyen TP, Le QV, Dao DV, Ahn SH, Kim SY. Facile route for synthesizing WS_2/W_2C nano hollow flowers and their application for hydrogen evolution reaction. J Alloys Compd 2023;955:170231.

[93] Feng B, Jin S, Lang J, Wang J, Hua J, Sun Y, et al. FeS nanosheets assembled with 1T-MoS_2 nanoflowers on iron foam for efficient overall water splitting. CrystEngComm 2024;26:2269–76.

[94] Maurya PK, Mishra AK. In situ grown vertically oriented wrinkled $MoSe_2$ nanosheets over different substrates as bifunctional electrocatalysts for water splitting. ACS Appl Energy Mater 2024;7:487–98.

[95] An T, Wang Y, Tang J, Wei W, Cui X, Alenizi AM, et al. Interlaced NiS_2–MoS_2 nanoflake-nanowires as efficient hydrogen evolution electrocatalysts in basic solutions. J Mater Chem A 2016;4:13439–43.

[96] Nguyen TP, Nguyen DLT, Nguyen V-H, Le T-H, Ly QV, Vo D-VN, et al. Facile synthesis of WS_2 hollow spheres and their hydrogen evolution reaction performance. Appl Surf Sci 2020;505:144574.

[97] Li M, Zhou Z, Hu L, Wang S, Zhou Y, Zhu R, et al. Hydrazine hydrate intercalated 1T-Dominant MoS_2 with superior ambient stability for highly efficient electrocatalytic applications. ACS Appl Mater Interfaces 2022;14:16338–47.

[98] Marinov AD, Bravo Priegue L, Shah AR, Miller TS, Howard CA, Hinds G, et al. Ex situ characterization of 1T/2H MoS_2 and their carbon composites for energy applications, a review. ACS Nano 2023;17:5163–86.

[99] Zhang Y, Zhang S, He Y, Li H, He T, Shi H, et al. Self-supporting $MoSe_2$/$CoSe_2$@CFP electrocatalyst electrode for high-efficiency HER under alkaline solution. J Solid State Chem 2021;298:122108.

[100] Yan Y, Xia B, Li N, Xu Z, Fisher A, Wang X. Vertically oriented MoS_2 and WS_2 nanosheets directly grown on carbon cloth as efficient and stable 3-dimensional hydrogen-evolving cathodes. J Mater Chem A 2015;3:131–5.

[101] Ghuman KK, Yadav S, Singh CV. Adsorption and dissociation of H_2O on monolayered MoS_2 edges: energetics and mechanism from ab initio simulations. J Phys Chem C 2015;119:6518–29.

[102] Li S, Wang S, Salamone MM, Robertson AW, Nayak S, Kim H, et al. Edge-enriched 2D MoS_2 thin films grown by chemical vapor deposition for enhanced catalytic performance. ACS Catal 2017;7:877–86.

[103] Li C, Zhu L, Li H, Li H, Wu Z, Liang C, et al. Dual surfactants applied in synthesis of $MoSe_2$ for high-efficiency hydrogen evolution reaction. J Alloys Compd 2021; 863:158092.

[104] Liu Z, Nie K, Qu X, Li X, Li B, Yuan Y, et al. General Bottom-Up colloidal synthesis of nano-monolayer transition-metal dichalcogenides with high 1T′-Phase purity. J Am Chem Soc 2022;144:4863–73.

[105] Nguyen TP, Kim SY, Lee TH, Jang HW, Le QV, Kim IT. Facile synthesis of W_2C@WS_2 alloy nanoflowers and their hydrogen generation performance. Appl Surf Sci 2020;504:144389.

[106] Nguyen TV, Huynh KA, Le QV, Ahn SH, Kim SY. Facile synthesis of WS_2/WO_3 materials in a batch reactor for the hydrogen evolution reaction. Int J Energy Res 2024;2024:4878549.

[107] Nguyen TV, Tekalgne M, Tran CV, Nguyen TP, Dao V, Le QV, et al. Synthesis of MoS_2/WS_2 nanoflower heterostructures for hydrogen evolution reaction. Int J Energy Res 2024;2024:3192642.

[108] Do HH, Le QV, Lee TH, Hong SH, Ahn SH, Jang HW, et al. Core-shell architecture of $NiSe_2$ nanoparticles@nitrogen-doped carbon for hydrogen evolution reaction in acidic and alkaline media. Int J Energy Res 2021;45:20463–73.

[109] Janani G, Surendran S, Lee D-K, Shanmugapriya S, Lee H, Subramanian Y, et al. Aggregation induced edge sites actuation of 3D MoSe2/rGO electrocatalyst for high-performing water splitting system. Aggregate 2024;5:e430.

[110] Zhao X, Shang Z, Li N, Lu Q, Guo E, Wei M, et al. NH4F-induced morphology-dependent $NiSe_2$/CoSe electrocatalysts on Ni foam for enhanced overall water splitting. J Colloid Interface Sci 2025;693:137642.

[111] Aggarwal P, Sarkar D, Dwivedi PK, Menezes PW, Awasthi K. Deciphering the influence of morphology and crystal structure on alkaline hydrogen evolution activity in polymorphic cobalt diselenide. ACS Appl Energy Mater 2024;7: 1550–60.

[112] Kwon IS, Kwak IH, Debela TT, Abbas HG, Park YC, Ahn J-p, et al. Se-Rich $MoSe_2$ nanosheets and their superior electrocatalytic performance for hydrogen evolution reaction. ACS Nano 2020;14:6295–304.

[113] Liu Z, Sun Z, Qu X, Nie K, Yang Y, Li B, et al. Solution-processable microstructuring of 1T′-Phase Janus MoSSe monolayers for boosted hydrogen production. J Am Chem Soc 2024;146:23252–64.

[114] Shaikh N, Mukhopadhyay I, Ray A. Hydrothermally grown MoS_2 nanosheets under non-equilibrium condition and its electrocatalytic hydrogen evolution performance. J Mater Res 2022;37:1892–903.

[115] Yang C, Zhou L, Wang C, Duan W, Zhang L, Zhang F, et al. Large-scale synthetic Mo@(2H-1T)-$MoSe_2$ monolithic electrode for efficient hydrogen evolution in all pH scale ranges and seawater. Appl Catal, B 2022;304:120993.

[116] Zhan W, Zhai X, Li Y, Wang M, Wang H, Wu L, et al. Regulating local atomic environment around vacancies for efficient hydrogen evolution. ACS Nano 2024; 18:10312–23.

[117] Chen B-A, Rowberg AJE, Pham TA, Ogitsu T, Kamat PV, Ptasinska S. Reactivity of sulfur vacancy-rich MoS_2 to water dissociation. J Phys Chem C 2024;128: 10379–87.

[118] Li G, Zhang D, Qiao Q, Yu Y, Peterson D, Zafar A, et al. All the catalytic active sites of MoS_2 for hydrogen evolution. J Am Chem Soc 2016;138:16632–8.

[119] Cheng Y, Song H, Wu H, Zhang P, Tang Z, Lu S. Defects enhance the electrocatalytic hydrogen evolution properties of MoS_2-based materials. Chem Asian J 2020;15:3123–34.

[120] Perivoliotis DK, Ekspong J, Zhao X, Hu G, Wågberg T, Gracia-Espino E. Recent progress on defect-rich electrocatalysts for hydrogen and oxygen evolution reactions. Nano Today 2023;50:101883.

[121] Zhu J, Wang Z, Yu H, Li N, Zhang J, Meng J, et al. Argon plasma induced phase transition in monolayer MoS_2. J Am Chem Soc 2017;139:10216–9.

[122] Bussolotti F, Yang J, Kawai H, Wong CPY, Goh KEJ. Impact of S-Vacancies on the charge injection barrier at the electrical contact with the MoS_2 monolayer. ACS Nano 2021;15:2686–97.

[123] Kang G, Hong D, Kim J-Y, Lee G-D, Lee S, Nam D-H, et al. Phase engineering of transition metal dichalcogenides via a thermodynamically designed gas–solid reaction. J Phys Chem Lett 2021;12:8430–9.

[124] Zhang W, Wang K, Tian Y, Liao L, Liu H. High hydrogen evolution reaction performance of MoS2 nanosheets with sulfur vacancies synthesized from natural molybdenite. J Mater Sci 2025;60:3321–32.

[125] Yin Y, Han J, Zhang Y, Zhang X, Xu P, Yuan Q, et al. Contributions of phase, sulfur vacancies, and edges to the hydrogen evolution reaction catalytic activity of porous molybdenum disulfide nanosheets. J Am Chem Soc 2016;138:7965–72.

[126] Fruehwald HM, Liebsch Y, Javed U, Lebius H, Grygiel C, Rahali R, et al. Basal-plane pores activate monolayer MoS_2 for the hydrogen evolution reaction. ACS Catal 2025;15:3768–76.

[127] Xiao D, Ruan Q, Bao D-L, Luo Y, Huang C, Tang S, et al. Effects of ion energy and density on the plasma etching-induced surface area, edge electrical field, and multivacancies in $MoSe_2$ nanosheets for enhancement of the hydrogen evolution reaction. Small 2020;16:2001470.

[128] Jin J, Wang X, Hu Y, Zhang Z, Liu H, Yin J, et al. Precisely control relationship between sulfur vacancy and H absorption for boosting hydrogen evolution reaction. Nano-Micro Lett 2024;16:63.

[129] Guo G, Liu J, Liu N, Zhao J, Liao J. Construction of sulfur-rich vacancies MoS_2 and Ni_3S_2 heterojunction for efficient hydrogen evolution reaction. Int J Hydrogen Energy 2025;145:832–40.

[130] Ren X, Wu F, Wang Y, Ou Q, Li F. Confined synthesis of edge-rich V-doped $MoSe_2$ nanosheets on carbon black for advanced hydrogen evolution reaction. New J Chem 2024;48:5160–6.

[131] Zhou H, Zhang W, Li L, Sun F, Hong A. Doping engineering: highly improving hydrogen evolution reaction performance of monolayer SnSe. Int J Hydrogen Energy 2021;46:37907–14.

[132] Dinh KN, Sun Y, Pei Z, Yuan Z, Suwardi A, Huang Q, et al. Electronic modulation of nickel disulfide toward efficient water electrolysis. Small 2020;16:1905885.

[133] Zheng H, Wang Q-N, Wang Z, Ma W, Long G, Chang B, et al. H_2 evolution with silicotungstic acid electron mediator over V-Doped MoS_2 electrocatalysts. ACS Energy Lett 2025;10:678–84.

[134] Xue J-Y, Li F-L, Zhao Z-Y, Li C, Ni C-Y, Gu H-W, et al. In situ generation of bifunctional Fe-Doped MoS_2 nanocanopies for efficient electrocatalytic water splitting. Inorg Chem 2019;58:11202–9.

[135] Deng J, Li H, Wang S, Ding D, Chen M, Liu C, et al. Multiscale structural and electronic control of molybdenum disulfide foam for highly efficient hydrogen production. Nat Commun 2017;8:14430.

[136] Liang T, Jia H, Zhou Y, Fan J, Xu Y, Hu Y, et al. A facile approach to enhance the hydrogen evolution reaction of electrodeposited MoS^{-2} in acidic solutions. New J Chem 2022;46:23344–50.

[137] Ghanashyam G, Kim H. Co-doped 1T-MoS_2 microspheres embedded in N-doped reduced graphene oxide for efficient electrocatalysis toward hydrogen and oxygen evolution reactions. J Power Sources 2024;596:234088.

[138] Li M, Min J, Huang Y, Meng L, Dong Z, Wang S, et al. Space-confinement and in situ reduction of Pt with 1T-MoS_2 for exceptional hydrogen evolution reaction in simulated seawater. ACS Appl Mater Interfaces 2024;16:69199–209.

[139] Zhang L, Li J, Yang Z, Sun L, Chen G, An W, et al. Phosphorus-doping-induced optimization of atomic hydrogen binding energy in $MoSe_2$ under high coverage for efficient electrocatalytic hydrogen evolution reactions. ChemistrySelect 2021;6:1305–12.

[140] Gao J, Ma H, Luo X, Yu L, Gu X, Liu J. Boosting electrocatalytic activity of $NiSe_2$ nanosheets by anion-cation dual-doping for highly efficient hydrogen evolution reaction. J Alloys Compd 2023;933:167793.

[141] Huang Y, Li M, Liu Z, Lin C-H, Guan P, Feng Z, et al. Construction of Co/Co_2P/VN heterointerfaces enhances trifunctional hydrogen and oxygen catalytic reactions. J Mater Chem A 2024;12:31883–94.

[142] Pi C, Li X, Zhang X, Song H, Zheng Y, Gao B, et al. In-Plane mott–schottky effects enabling efficient hydrogen evolution from Mo_5N_6-MoS_2 heterojunction nanosheets in Universal-pH electrolytes. Small 2022;18.

[143] Wang Z, Zhou T, Chen Z, Gu R, Tao J, Fan Z, et al. Three-dimensional strawlike $MoSe_2$-Ni(Fe)Se electrocatalysts for overall water splitting. Inorg Chem 2023;62:2894–904.

[144] Inta HR, Ghosh S, Mondal A, Tudu G, Koppisetti HVSRM, Mahalingam V. $Ni_{0.85}Se$/$MoSe_2$ interfacial structure: an efficient electrocatalyst for alkaline hydrogen evolution reaction. ACS Appl Energy Mater 2021;4:2828–37.

[145] Yan R, Luan T, Liu Z, Cao Y, Chi K, Yang S, et al. Co_9S_8/MnS/MoS_2 heterostructure grown in situ on Ni foam as highly efficient electrocatalysts for overall water splitting. Int J Hydrogen Energy 2025;98:14–24.

[146] Xie W, Liu K, Shi G, Fu X, Chen X, Fan Z, et al. CoS_2 nanowires supported graphdiyne for highly efficient hydrogen evolution reaction. J Energy Chem 2021;60:272–8.

[147] Poudel MB, Logeshwaran N, Prabhakaran S, Kim AR, Kim DH, Yoo DJ. Low-cost hydrogen production from alkaline/seawater over a single-step synthesis of Mo_3Se_4-NiSe core–shell nanowire arrays. Adv Mater 2024;36:2305813.

[148] Zhao G, Li P, Rui K, Chen Y, Dou SX, Sun W. $CoSe_2$/$MoSe_2$ heterostructures with enriched water adsorption/dissociation sites towards enhanced alkaline hydrogen evolution reaction. Chem Eur J 2018;24:11158–65.

[149] Basu M. Nanotubes of $NiCo_2S_4$/Co_9S_8 heterostructure: efficient hydrogen evolution catalyst in alkaline medium. Chem Asian J 2018;13:3204–11.

[150] M P, Nj H, Dongre SS, Sahoo SK, Balakrishna RG, R S. NiMo LDH-derived Mo@$NiSe_2$ as advanced electrocatalysts for hydrogen evolution in acidic and alkaline systems. Energy Fuels 2025;39:6930–41.

[151] Qi Y, Chen J, Liu D, Wei X, Qu L, Huang C, et al. Self-supported bimetallic selenide heterostructure catalyst with enhanced electronic interaction for industrial-level seawater electrolysis. Chem Eng J 2025;512:162567.

[152] Li Y, Du H, Su Y, Zhao J, Qu K, Zhang X, et al. Construction of heterostructured NiS/$NiSe_2$ and their application in electrocatalytic water splitting. Int J Hydrogen Energy 2024;66:286–93.

[153] Rehman B, Kimbulapitiya KMMDK, Date M, Chen C-T, Cyu R-H, Peng Y-R, et al. Rational design of phase-engineered WS_2/WSe_2 heterostructures by low-temperature plasma-assisted sulfurization and selenization toward enhanced HER performance. ACS Appl Mater Interfaces 2024;16:32490–502.

[154] Liu Z, Wang T, Chang P, Guan L, Wang X, Xu C, et al. MOF-derived MoS_2@o-$CoSe_2$ hetero-catalysts accompanied by structural phase transition for efficient electrochemical hydrogen production. Int J Hydrogen Energy 2024;51:119–32.

[155] Zhang L, Wang T, Sun L, Sun Y, Hu T, Xu K, et al. Hydrothermal synthesis of 3D hierarchical $MoSe_2$/$NiSe_2$ composite nanowires on carbon fiber paper and their enhanced electrocatalytic activity for the hydrogen evolution reaction. J Mater Chem A 2017;5:19752–9.

[156] Yang D, Liu Y, Wang B, He J, Chen Y. $NiSe_2$ nanocrystals anchored graphene nanosheets as highly efficient and stable electrocatalyst for hydrogen evolution reaction in alkaline medium. J Alloys Compd 2019;792:789–96.

[157] Kim M, Anjum MAR, Lee M, Lee BJ, Lee JS. Activating MoS_2 basal plane with Ni_2P nanoparticles for Pt-Like hydrogen evolution reaction in acidic media. Adv Funct Mater 2019;29:1809151.

[158] Do HH, Nguyen CC, Nguyen DLT, Ahn SH, Kim SY, Le QV. MOF-derived $NiSe_2$ nanoparticles grown on carbon fiber as a binder-free and efficient catalyst for hydrogen evolution reaction. Int J Hydrogen Energy 2022.

[159] Najafi L, Bellani S, Oropesa-Nuñez R, Prato M, Martín-García B, Brescia R, et al. Carbon nanotube-supported $MoSe_2$ holey Flake:Mo_2C ball hybrids for bifunctional pH-Universal water splitting. ACS Nano 2019;13:3162–76.

[160] Huang Y, Li M, Liang T, Zhou Y, Guan P, Zhou L, et al. Structural optimization and electrocatalytic hydrogen production performance of carbon-based composites: a mini-review. Carbon Trends 2024;15:100363.

[161] Xu W, Zhang D, Wang T, Lai J, Wang L. Non-platinum-based electrocatalysts for high performance acidic hydrogen evolution reactions in proton exchange membrane water electrolysis. Appl Catal B Environ Energy 2025;361:124626.

[162] Nie K, Li N, Li B, Yuan Y, Zhang Y, Liu P, et al. Well-ordered single-atomic cobalt-1T-MoS_2/C superlattice heterostructure toward durable overall water splitting. Chem Eng J 2023;475:146066.

[163] Chen Y, Meng G, Yang T, Chen C, Chang Z, Kong F, et al. Interfacial engineering of Co-doped 1T-MoS_2 coupled with V_2C MXene for efficient electrocatalytic hydrogen evolution. Chem Eng J 2022;450:138157.

[164] Li J, Zhang C, Ma H, Wang T, Guo Z, Yang Y, et al. Modulating interfacial charge distribution of single atoms confined in molybdenum phosphosulfide heterostructures for high efficiency hydrogen evolution. Chem Eng J 2021;414:128834.

[165] Gu R, Zhou T, Wang Z, Chen Z, Tao J, Fan Z, et al. Mo/P doped NiFeSe as bifunctional electrocatalysts for overall water splitting. Int J Hydrogen Energy 2023;48:27642–51.

[166] Jiang F, Wang Y, Peng H, Wu Y, Zhang Z, Li Y, et al. Triggering asymmetric hybridization via ni-se-co electron bridges on rich amorphous heterostructured nickel selenide for durable alkaline water splitting. Appl Catal B Environ Energy 2025;372:125326.

[167] Yi L, Nie K, Li B, Zhang Y, Hu C, Hao X, et al. Tailoring copper single-atoms-stabilized metastable transition-metal-dichalcogenides for sustainable hydrogen production. Angew Chem Int Ed 2025;64:e202414701.

[168] Wang T, Zhang X, Yu X, Li J, Liu Z, Zhang Y, et al. Regulating charge redistribution and active species in vanadium disulfide for boosting hydrazine-assisted alkaline water splitting. J Colloid Interface Sci 2025;700:138312.

[169] Hu M, Qian Y, Zhang R, Guo C, Yang L, Li L. Interfacial electronic modulation of NiCo decorated nano-flowered MoS_2 on carbonized wood as a remarkable bifunctional electrocatalyst for boosting overall water splitting. J Colloid Interface Sci 2025;677:729–38.

[170] Zhang N, Yang X, Pei Q, Gao M, Liu X, Tang R, et al. Activating the few-layer and short-range order 1T-MoS_2 via interface engineering for efficient alkaline hydrogen evolution. Int J Hydrogen Energy 2026;200:152893.

[171] Dai T-J, Sun J, Peng X-S, Gong J-N, Zhou Z-Y, Wang X-Q. In situ synthesis of heterogeneous $NiSe_2$/$MoSe_2$ nanocomposite for high-efficiency electrocatalytic hydrogen evolution reaction. Energy Sci Eng 2022;10:4061–70.

[172] Abdul M, Ko C, Tang X, Ismail MA, Khalifa SB, Saidani T, et al. Bifunctional Nd_2Se_3–Mn_2O_3 heterostructure nanospheres for enhanced alkaline water splitting via interface engineering. Int J Hydrogen Energy 2025;144:303–14.

[173] Ren M, Feng G, Khalifa SB, Alsaif NAM, Chebaane S, Ismail MA, et al. Development of bifunctional synergistic $MoSe_2$-Ni_3S_2 heterostructure catalyst towards overall water splitting in alkaline medium. Fuel 2026;407:137408.

[174] Hu P, Li S, Qu J, Zhou J, Wang Z, Wang Y, et al. Activating the hydrogen evolution and overall water splitting performance of stable highly efficiency V doped $NiMoSe_x$ electrocatalyst by a selenization process. Int J Hydrogen Energy 2025;158:150501.